MATCHED INTERFACE AND BOUNDARY ENHANCED (MIB) MULTIRESOLUTION TIME-DOMAIN ALGORITHM FOR ELECTROMAGNETIC SIMULATIONS

by

PENGFEI YAO

SHAN ZHAO, COMMITTEE CHAIR
JOSEPH NEGGERS
DAVID HALPERN
TSUN ZEE MAI
FEI HU

A DISSERTATION

Submitted in partial fulfillment of the requirements
for the degree of Doctor of Philosophy
in the Department of Mathematics
in the Graduate School of
The University of Alabama

TUSCALOOSA, ALABAMA

2011

Copyright Pengfei Yao 2011
ALL RIGHTS RESERVED

ABSTRACT

The present work introduces a new boundary closure treatment for the wavelet based multiresolution time-domain (MRTD) solution of Maxwell's equations [**1**]. Accommodating nontrivial boundary conditions, such as the Robin condition or time dependent condition, has been a challenging issue in the MRTD analysis of wave scattering, radiation, and propagation. A matched interface and boundary multiresolution time-domain (MIB-MRTD) method is introduced to overcome this difficulty. Several numerical benchmark tests are carried out to valid the MIB-MRTD method. Dispersion and stability analysis for the MIB-MRTD method are conducted and compared with the high-order finite difference time-domain (FDTD) method . The proposed boundary treatment can also be applied to other high order approaches, such as the dispersion-relation-preserving (DRP) method. The MIB boundary scheme greatly enhances the feasibility for applying the MRTD methods to more complicated electromagnetic structures.

DEDICATION

This dissertation is dedicated to everyone who helped me and guided me through the trial of creating this manuscript. In particular, my family and close friends who stood by me throughout the time taken to complete this work.

ACKNOWLEDGMENTS

I would like to thank my advisor, Dr. Shan Zhao, for all of his help throughout these years. As a mentor, Dr. Zhao is a great motivator and educator. I consider it an honor and privilege to have been mentored by him.

I would also like to thank my committee members, Dr. Joseph Neggers, Dr. David Halpern, Dr. Mai Tsun Zee and Dr. Fei Hu for their support of both the dissertation and my academic progress.

I thank Dr. Zhijian Wu and other Math Department faculty and staff for their invaluable help. They were always willing and eager to give me a hand when needed.

CONTENTS

ABSTRACT ii

DEDICATION iii

ACKNOWLEDGMENTS iv

LIST OF TABLES vii

LIST OF FIGURES viii

CHAPTER 1. INTRODUCTION 1

CHAPTER 2. GOVERNING EQUATIONS 6

2.1. Electromagnetism and Maxwells Equations 6

2.2. Maxwells Equations in Three Dimensions 7

2.3. Reduction to TMz and TEz Modes 8

2.4. Reduction to One Dimension 9

2.5. Perfect Electric and Perfect Magnetic Conductors 10

2.6. A Perfect Matched Layer 11

CHAPTER 3. THEORY AND ALGORITHM 13

3.1. Multiresolution Time-Domain (MRTD) Analysis 13

3.2. Spatial Discretization 16

3.3. Image principle 20

3.4. Matched interface and boundary (MIB) treatment 22

CHAPTER 4. NUMERICAL DISPERSION ANALYSIS 26

4.1. One Dimensional Scalar Wave Equation 26

4.2. The Dispersion Relation for The One-Dimensional Wave Equation 27

4.3. Numerical Dispersion Relation 28
4.4. A Fourier Analysis of The Computational Errors 31
4.5. An Example: The One-Way Wave Equation 33

CHAPTER 5. NUMERICAL STABILITY ANALYSIS 35
5.1. Discretization Matrix 35
5.2. Courant - Friedrichs - Levy (CFL) Number 38

CHAPTER 6. NUMERICAL EXPERIMENTS 43
6.1. A Hollow Rectangular Waveguide 43
6.2. A Shifted Computational Domain 48
6.3. A Rectangular Open Cavity 51
6.4. A Test Without An Analytical Solution 55

CHAPTER 7. CONCLUSION AND FUTURE WORK 59

BIBLIOGRAPHY 62
APPENDIX 65

LIST OF TABLES

1. Coefficients for The CDF-MRTD Scheme 18
2. Spectral Radius of MIB-MRTD Matrix 41
3. CFL Number for One-Dimensional Wave Equation 42
4. The MRTD Results of Example (1) by Using The Image Principle 45
5. The MRTD Results of Example (1) by Using The MIB Scheme 45
6. The Results of The MIB-MRTD Method for Example (2) 51
7. The Results of The MIB-MRTD Method for Example (3) 53
8. The Results of The MIB-MRTD Method for Example (4) 56

LIST OF FIGURES

1. Propagation of An Electromagnetic Wave 8
2. PML Boundaries 12
3. Haar Wavelet 14
4. Daubechies Wavelet 15
5. Electromagnetic Fields in Two Dimensions 17
6. An Illustration of The Image Principle 21
7. An Illustration of The MIB Grid Partition and The Iterative Procedure 24
8. Numerical Dispersion Errors at Different Frequencies 32
9. One-Way Wave Equation 34
10. Discretization Matrix of The MIB-MRTD Method 36
11. Dicretization Matrix of The One-Dimensional Wave Equation 37
12. Stable Region of The Runge-Kutta Method 38
13. Eigenvalues of The MIB-MRTD Discretization Matrix 40
14. Spurious Modes 42
15. A Perfect Electric Conductor 44
16. The Numerical Convergence Rate of The MIB-MRTD Method (1) 46
17. Matlab Simulations of E_z for Example (1) 48
18. A Shifted Computational Domain 49
19. The Numerical Convergence Rate of The MIB-MRTD Method (2) 50
20. An Open Cavity 51
21. The Numerical Convergence Rate of The MIB-MRTD Method (3) 54
22. Matlab Simulations of E_z for Example (3) 55
23. The Numerical Convergence Rate of The MIB-MRTD Method (4) 57
24. Matlab Simulations of E_z for Example (4) 58

CHAPTER 1

INTRODUCTION

Maxwell's equations have been served as the foundation of electromagnetics in the past over one hundred years. Those equations represent a perfect unification of electric and magnetic fields and provide explanations of all kinds of wave propagation, radiation and scattering phenomena. The numerical solutions and simulations of those equations have brought numerous great innovations in scientific and technological areas such as micro devices, optical devices, antennas, aircraft radar signature, and telecommunication chips. In Yee's [**2**] seminal paper, a Finite-Difference-Time-Domain (FDTD) method was initially proposed for solving one, two and three dimensional Maxwell's equations. It can be seen that the change in the electric field in time (the time derivative) depends on the change in the magnetic field across space. This results in the basic FDTD time-stepping relation that, at any point in space, the updated value of the electric field in time depends on the stored value of the electric field and the numerical curl of the local distribution of the magnetic field in space. Yee's FDTD method has proven to be a powerful numerical technique for its simplicity, high performance in stability and modeling versatility. However, it suffers from limitations to electromagnetic problems involving electrically large structures. Typically, the dimensions of the scatter in such problems greatly exceed the wavelength of the incident wave so that the grid size required by using the FDTD method could become prohibitively expensive. In order to circumvent this difficulty, numerical approaches that are able to accurately represent the wave solution by using only a few points per wavelength must be employed to relieve the computational cost. This motivates the development of many low dispersion or high order FDTD methods in the past two decades, such as FDTD(2,4) scheme [**3**] and dispersion-relation-preserving (DRP) FDTD methods [**4, 5**],

On the other hand, the moment methods introduced by R.F. Harrington [**6**] provide mathematical approaches for the discretization of partial differential equations using orthonormal basis functions. The use of scaling and wavelet functions as a complete set of basis functions lead to new time-domain schemes called multiresolution time-domain (MRTD) methods [**7, 8**]. When electromagnetic fields are expanded solely in terms of scaling functions, the corresponding MRTD scheme is usually called as an S-MRTD scheme, while W-MRTD scheme refers to a scheme in which both scaling and wavelet functions are used as basis functions. The original MRTD methods are derived using cubic spline Battle-Lemarie scaling and wavelet functions. The Battle-Lemarie wavelets present good smoothness properties, but they also have the noncompact disadvantage. This means that many neighboring terms must be included in the update equation at each node to ensure the numerical accuracy. The Haar wavelet family yields a simple algorithm but is lack of smoothness. In fact, it can be shown that an n-level Haar wavelet expansion is equivalent to the Yee's FDTD scheme of 2^n resolution. Various different MRTD methods using compactly supported wavelet expansions have been developed in the literature. For example, novel MRTD methods based on Coifman and Daubechies scaling functions have been introduced, respectively, in [**9**] and [**10**]. A general framework for constructing MRTD algorithms based on biorthogonal scaling and wavelet functions has been established in [**11**], with a particular realization given to the Cohen-Daubechies-Feauveau (CDF) biorthogonal wavelets. The stencil length of the Daubechies type MRTD methods can be adjusted by the number of vanishing moments, while the latter also determines the order of accuracy of the resulting MRTD spatial discretization [**12**]. In [**13**], a systematic procedure is proposed to update the time in the MRTD calculations by using a new Runge-Kutta scheme so that an arbitrarily high order of convergence in both space and time could be realized.

The capability of accommodating various boundary conditions is another major issue in computational electromagnetics (CEM). For example, high-order finite difference methods use wide stencils (for example, an eighth order of accuracy method requires nine successive

sample points on the grid). Thus to maintain a designed high order accuracy, special boundary treatments are required when these finite difference kernels refer to nodes outside the computational domain. However, it is numerically challenging to contrive a boundary closure method which is not only highly accurate to maintain the designed level of accuracy, but also sufficiently robust to handle various boundary conditions such as perfectly matched layer (PML) absorbing boundary condition [**14**], perfect electric conducting (PEC) and perfect magnetic conducting (PMC) boundary conditions. A PML is an artificial absorbing layer for waveguides (a structure, commonly meaning a hollow conductive metal pipe, used to guide waves), commonly used to simulate computational domains with open boundaries, especially in the FDTD and finite element (FEM) methods. The key property of a PML is that there is no reflection at the interface when the incident waves transfer from the PML to a non-PML medium. This property allows the PML to strongly absorb outgoing waves from the interior of a computational domain without reflecting them back into the interior. PEC and PMC are idealized conductors having very high electrical permittivities and magnetic permeabilities respectively, which allow tangential components of the electric and magnetic fields to be continuous across any interface. Therefore, the development of such a boundary closure scheme is very necessary for handling complicated boundary conditions in scientific and engineering computations.

The boundary closure of wide-stencil high-order methods can be carried out in essentially two ways: one is to employ the information on a small fictitious domain outside the boundary, while the other relies only on the information inside the boundary. Many different types of boundary closure methods have been proposed to incorporate with the core high-order methods. For example, one type method builds boundary conditions into differentiation kernels [**15**], so that both the differential equation and its boundary conditions can be satisfied simultaneously. However, this technique may not be robust enough to handle general boundary conditions. The most widely used boundary closure method for high order approaches is to employ more asymmetric differential kernels near the boundary such as the one-side finite difference (OFD) method. These treatments do not refer to nodes

outside the computational domain. Thus they require very dense spatial discretization near the boundary to maintain a overall high accuracy.

It is of considerable interest to study other types of boundary closure methods, treatment of boundary conditions using fictitious points outside computational domain. The image principle [**16**] assumes there is one-to-one correspondence between the inner nodes and the outer fictitious points on the boundary. This fictitious domain boundary method handles well many boundary conditions. However, it has limitations to accommodate some complex boundary conditions, such as the Robin condition, because under such occasions, the one-to-one assumption might not be rigorously valid. Therefore, a new matched interface and boundary (MIB) method [**17, 18**] is formulated to handle more general and complex boundary conditions. The MIB method repeatedly utilized the given boundary conditions to determine as many fictitious points as needed in a high-order scheme. A MIB hierarchical derivative matching [**19, 20**] scheme is proposed for simulation of electromagnetic wave scattering and propagation in inhomogeneous media. More recently, high-order MIB schemes for elliptic interface problems with curved interfaces have been constructed [**21**] as a generalization of the immersed interface method (IIM) [**22**]. In those work, fictitious points are determined iteratively by solving several coupled algebraic equation associated with the imposed interface conditions. Therefore, higher order accuracy can be realized without significant increase of numerical complexity and computational cost.

The present work is to construct a general procedure to implement nontrivial boundary conditions in the MRTD discretization. This is accomplished by introducing a fictitious domain boundary closure via the MIB method. For regular domain with straight boundaries, the MIB boundary scheme has been constructed for supporting arbitrarily high order central finite difference methods [**17, 18**]. In the present study, to illustrate the proposed boundary closure scheme, the CDF S-MRTD method [**11**] will be employed. We note that the proposed procedure can be extended to other S-MRTD and W-MRTD methods. The rest of the dissertation is organized as the follows. In Chapter 2, a brief introduction of Maxwell's equations is laid out. Several important modes in electromagnetics are introduced for further

consideration. Chapter 3 is devoted to the theories and formulations of the MRTD and MIB methods. In Chapter 4, a Fourier based dispersion error analysis is conducted for the present MIB-MRTD method. We discuss the stability performance of the MIB-MRTD from a matrix structure perspective in Chapter 5 and numerical tests involving Robin and time-dependent boundary conditions are carried out to validate the proposed method in Chapter 6. Finally, a conclusion ends this dissertation.

CHAPTER 2

GOVERNING EQUATIONS

2.1. Electromagnetism and Maxwell's Equations

Electromagnetism is the study of the electric and magnetic phenomena caused by electric charges at rest or in motion. There two kinds of electric charges, positive and negative, following a definition given by *Benjamin Franklin* [**23**]. Both positive and negative charges are sources of an electric field intensity E. Moving charges produce a current that can further give rise to a magnetic field intensity H. A vector field is defined as a spatial distribution of a vector quantity, which may or may not be function of time. A time-varying electric field intensity is always accompanied by a magnetic field intensity and vice versa. In other words, time-varying electric and magnetic field intensities are intrinsically coupled and result in an electromagnetic field intensity. Time-dependent electromagnetic field intensities produce waves that radiate from their source toward an observation point. In our study of electromagnetic wave propagation in a waveguide, we will see that the boundary condition at a conducting surface requires a charge density distribution to support the electric and magnetic field intensities defined by *Maxwell's Equations*.

Maxwell's Equations in differential form

$$\nabla \times E = -\frac{\partial B}{\partial t} \tag{2.1.1}$$

$$\nabla \times H = \frac{\partial B}{\partial t} + J \tag{2.1.2}$$

$$\nabla \cdot D = \rho_f \tag{2.1.3}$$

$$\nabla \cdot B = 0 \tag{2.1.4}$$

where B is the magnetic flux density, D is the electric flux density, J is the electric current density, and ρ_f is the free charge density, respectively.

2.2. Maxwell's Equations in Three Dimensions

In linear, isotropic, nondispersive materials (materials having field-independent, direction-independent, and frequency-independent electric and magnetic properties), we can relate D to E and B to H using simple proportions:

$$D = \epsilon E; \quad B = \mu H \tag{2.2.1}$$

where ϵ is the electrical permittivity and μ is the magnetic permeability. Assuming the absence of charge density and current source, we obtain the *Maxwell's* curl equations by substituting $Eq(2.2.1)$ into $Eq(2.1.1)$ and $Eq(2.1.2)$:

$$\epsilon \frac{\partial E}{\partial t} = \nabla \times H \tag{2.2.2}$$

$$\mu \frac{\partial H}{\partial t} = -\nabla \times E \tag{2.2.3}$$

We now write out the vector components of the curl operators of $Eq(2.2.2)$ and $Eq(2.2.3)$ in *Cartesian* coordinates. This yields the following system of six coupled scalar equations:

$$\begin{aligned}
\epsilon \frac{\partial E_x}{\partial t} &= \frac{\partial H_z}{\partial y} - \frac{\partial H_y}{\partial z} & \qquad \mu \frac{\partial H_x}{\partial t} &= \frac{\partial E_y}{\partial z} - \frac{\partial E_z}{\partial y} \\
\epsilon \frac{\partial E_y}{\partial t} &= \frac{\partial H_x}{\partial z} - \frac{\partial H_z}{\partial x} & \qquad \mu \frac{\partial H_y}{\partial t} &= \frac{\partial E_z}{\partial x} - \frac{\partial E_x}{\partial z} \\
\epsilon \frac{\partial E_z}{\partial t} &= \frac{\partial H_y}{\partial x} - \frac{\partial H_x}{\partial y} & \qquad \mu \frac{\partial H_z}{\partial t} &= \frac{\partial E_x}{\partial y} - \frac{\partial E_y}{\partial x}
\end{aligned} \tag{2.2.4}$$

The system of six coupled partial differential equations of $Eq(2.2.4)$ forms the basis of the numerical algorithms for electromagnetic wave interactions with general three-dimensional objects.

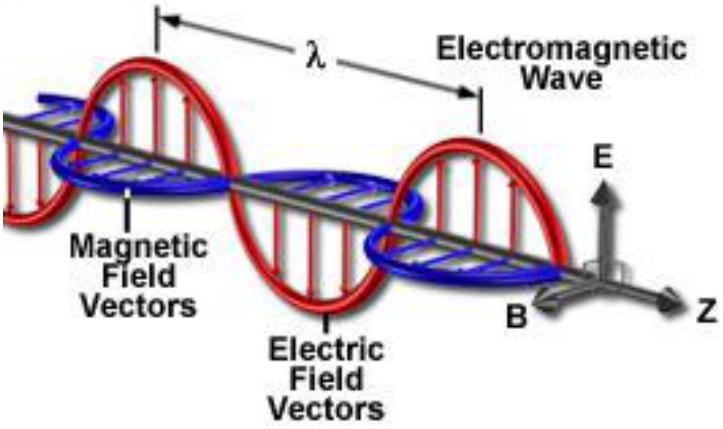

FIGURE 2.1. Propagation of an Electromagnetic Wave

2.3. Reduction to TM_z and TE_z Modes

Considering the wave propagation shown in $Fig(2.1)$, we assume that the structure being modeled extends to infinity in the z-direction with no change in its transverse cross section and the incident wave is also uniform in the z-direction. Then all partial derivatives of the fields with respect to z must be equal to zero. By grouping the three equations of $Eq(2.2.4)$ according to field components, we obtain the following set of equations which forms the *transverse magnetic mode with respect to z* (TM_z) in two dimensions:

$$\begin{aligned} \epsilon\frac{\partial E_z}{\partial t} &= \frac{\partial H_y}{\partial x} - \frac{\partial H_x}{\partial y} \\ \mu\frac{\partial H_x}{\partial t} &= -\frac{\partial E_z}{\partial y} \\ \mu\frac{\partial H_y}{\partial t} &= \frac{\partial E_z}{\partial x} \end{aligned} \tag{2.3.1}$$

where E and H are, respectively, the normalized electric and magnetic field intensities. Similarly, we group the other three equations in $Eq(2.2.4)$ to form set of equations for

transverse electric mode with respect to z (TE_z) in two dimensions:

$$\begin{aligned}\epsilon\frac{\partial E_x}{\partial t} &= \frac{\partial H_z}{\partial y}\\ \epsilon\frac{\partial E_y}{\partial t} &= -\frac{\partial H_z}{\partial x}\\ \mu\frac{\partial H_z}{\partial t} &= \frac{\partial E_x}{\partial y} - \frac{\partial E_y}{\partial x}\end{aligned} \tag{2.3.2}$$

2.4. Reduction to One Dimension

Let us further assume that neither the electromagnetic field excitation nor the modeled geometry has any variation in the $y-$direction. In effect, we assume that all field partial derivatives with respect to y and z equal zero, and the interaction structure consists of an infinite space having possible material layering in the $x-$direction. Then the two-dimensional TM_z mode of *Maxwell's* equations in rectangular coordinates can be reduced to:

$$\begin{aligned}\mu\frac{\partial H_y}{\partial t} &= \frac{\partial E_z}{\partial x}\\ \epsilon\frac{\partial E_z}{\partial t} &= \frac{\partial H_y}{\partial x}\end{aligned} \tag{2.4.1}$$

We designate the mode as an $x-$directed,$z-$polarized *transverse electromagnetic* (TEM) wave in one dimension.

Again assuming that all partial derivatives with respect to y equal zero, we obtain:

$$\begin{aligned}\epsilon\frac{\partial E_y}{\partial t} &= -\frac{\partial H_z}{\partial x}\\ \mu\frac{\partial H_z}{\partial t} &= -\frac{\partial E_z}{\partial x}\end{aligned} \tag{2.4.2}$$

as an $x-$directed, $y-$polarized TEM wave in one dimension.

2.5. Perfect Electric and Magnetic Conductors

Perfect electric conductors (PEC) and perfect magnetic conductors (PMC) are two fundamental concepts in electromagnetic theory [**24**]. A PEC is an idealized conductor which

has very high electrical permittivity. It can be defined as a material in which two of the electromagnetic vectors vanish:

$$E = 0, \quad B = 0 \tag{2.5.1}$$

while there is no restriction to the other two vectors H and D. Similarly, A PMC is an idealized conductor which has very high magnetic permeability and can be defined as:

$$H = 0, \quad D = 0 \tag{2.5.2}$$

while E and B are not restricted. Because the tangential components of the E and H fields and the normal components of the D and B fields are continuous across any interface, the boundary conditions at the surfaces of a PEC and a PMC are:

$$\begin{aligned} n \cdot B = 0, \quad n \times E = 0 \\ n \cdot D = 0, \quad n \times H = 0 \end{aligned} \tag{2.5.3}$$

Here, n denotes the unit vector normal to the boundary. If the medium outside the body is isotropic, $Eq(2.5.3)$ can also be expressed as:

$$\begin{aligned} n \cdot H = 0, \quad n \times E = 0 \\ n \cdot E = 0, \quad n \times H = 0 \end{aligned} \tag{2.5.4}$$

respectively.

For example, one-dimensional *Maxwell's* $Eq(2.4.1)$ with PEC boundaries :

$$\begin{aligned} \mu \frac{\partial H_y}{\partial t} &= \frac{\partial E_z}{\partial x} \\ \epsilon \frac{\partial E_z}{\partial t} &= \frac{\partial H_y}{\partial x}, \quad (0 \le x \le 1) \\ E_z(0,t) = 0, \quad E_z(1,t) = 0, \quad E_z(x,0) &= E_z^0 \\ \frac{\partial H_y}{\partial x}(0,t) = 0, \quad \frac{\partial H_y}{\partial x}(1,t) = 0, \quad H_y(x,0) &= H_y^0 \end{aligned} \tag{2.5.5}$$

where E_z^0, H_y^0 are the initial values of the electric and magnetic fields.

2.6. A Perfect Matched Layer

A PML is an artifical absorbing layer for waveguides, commonly used to simulate computational domains with open boundaries. The key property of a PML is that there is no reflection at the interface when the incident waves transfer from the PML to a non-PML medium. This property allows the PML to strongly absorb outgoing waves from the interior of a computational domain without reflecting them back into the interior. PML was originally introduced by *Berenger* for use with *Maxwell's* equations. In the one-dimensional case, a PML is designed to absorb waves propagating in the x direction. The transformation for the x derivative $\frac{\partial}{\partial x}$ is given as:

$$\frac{\partial}{\partial x} = \frac{1}{1 + \frac{i\sigma(x)}{\omega}} \frac{\partial}{\partial x} \tag{2.6.1}$$

where σ is some function of x. Wherever σ is positive, propagating waves are attenuated. This can be illustrated by considering a sinusoidal-traveling-wave function $u(x,t) = e^{i(kx-\omega t)}$:

$$e^{i(kx-\omega t)} \rightarrow e^{i(kx-\omega t) - \frac{k}{\omega}\int^x \sigma(\tau)d\tau} \tag{2.6.2}$$

As shown in $Fig(2.2)$, waves are propagating in the field enclosed by the four PML boundaries. The region of interest is located at the center. All radiating waves will be absorbed when they reach the PML boundaries, which makes the field inside an ideal simulation for either the infinite space or the truncated space.

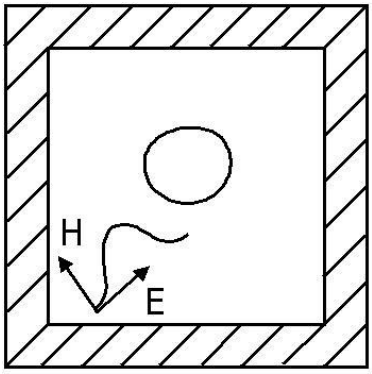

FIGURE 2.2. PML boundaries.

CHAPTER 3

THEORY AND ALGORITHM

3.1. Multiresolution Time-Domain (MRTD) Analysis

The Multiresolution Time-Domain method has been widely and successfully applied to various electromagnetic field problems, such as circuits [**26**] and microwave [**7**]cavities about which we will have a more detailed discussion. The MRTD can provide high-efficiency and high-accuracy spatial discretization by choosing appropriate wavelets. A wavelet is a brief oscillating waveform that lasts for at most a few cycles. Thus, wavelets are functions that satisfy certain mathematical requirements and are used in representing data or other functions. A function $\phi(t)$ is defined as a wavelet if:

1) The integral of $\phi(t)$ is zero

$$\int_{-\infty}^{\infty} \phi(t)dt = 0 \tag{3.1.1}$$

This means that a wavelet must have zero average value in the time domain and that the wavelet must be an oscillatory bandpass function.

2) The integral of $\phi^2(t)$ is unity

$$\int_{-\infty}^{\infty} \phi^2(t)dt = 1 \tag{3.1.2}$$

There are a number of functions that meet these requirements. Some popular wavelets include *Daubechies, Coifman, cubic-splines, Lemarie* and *Haar* wavelets. The choice of wavelet for computational purposes depends on the special properties of the wave being studied for.

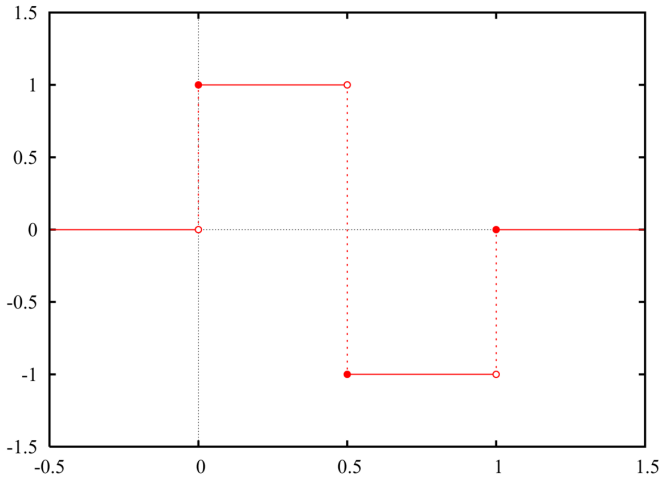

FIGURE 3.1. Haar Wavelet

Here we provide an example of the *Haar* wavelet. Let

$$\phi(t) = \begin{cases} 1, & 0 \leq t \leq 0.5 \\ -1, & 0.5 \leq t \leq 1 \\ 0, & \text{otherwise} \end{cases} \tag{3.1.3}$$

Each mother wavelet can be used to generate other wavelets to form a set of basis functions. This is achieved in the following manner

1) Translation and Scaling:

$$\phi(t) \to \phi(t+k) \tag{3.1.4}$$

$$\phi(t) \to \phi(mt) \tag{3.1.5}$$

where k is the translation factor and m is the scaling factor. Thus, other wavelets are generated from a single basic wavelet $\phi(t)$. This leads us to the third important property, orthogonality. The basis functions generated have to be orthogonal:

$$\int \phi_i(t)\phi_j(t)dt = \begin{cases} 1, & i = j \\ 0, & i \neq j \end{cases} \tag{3.1.6}$$

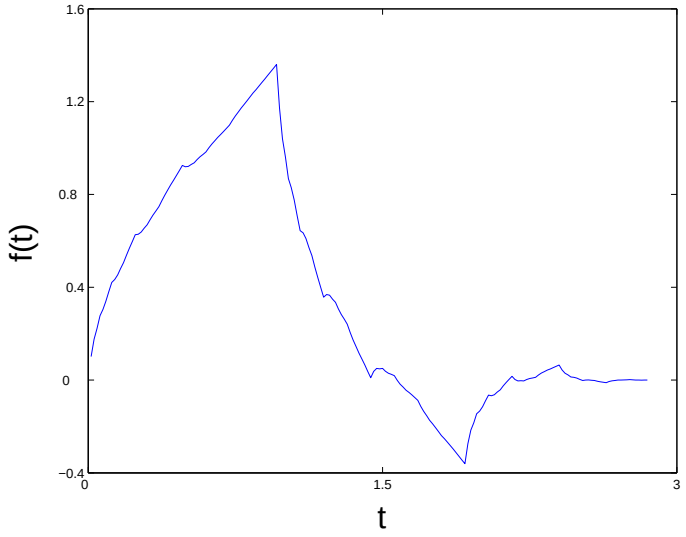

FIGURE 3.2. Daubechies Wavelet for $S = 2$

It is not a necessary requirement that the wavelets are orthogonal, but the use of orthogonal wavelets simplifies computation.

Next, we describe the *Daubechies* wavelets we used for our MIB-MRTD scheme. In order to obtain the coefficients for spatial discretization, we consider the following scaling equation: [**25**]

$$\phi(t) = \sum_{k=-\infty}^{\infty} a_k \phi(St - k) \tag{3.1.7}$$

The scaling factor $S = 2$ is selected as a convenient choice and the corresponding *Daubechies* wavelet function is shown in $Fig(3.2)$. The constant coefficients a_k are known as filter coefficients and are obtained by imposing some conditions on the scaling function. First, the scaling function has a nonvanishing integral

$$\int_{-\infty}^{\infty} \phi(t)dt = 1 \tag{3.1.8}$$

This leads to

$$\sum_{k=-\infty}^{\infty} a_k = 2 \tag{3.1.9}$$

Second, the scaling function is orthogonal to translations

$$\int_{-\infty}^{\infty} \phi(t)\phi(t+m)dt = \delta_{0,m} \tag{3.1.10}$$

This orthogonality condition implies that

$$\sum_{k=-\infty}^{\infty} a_k a_{k+2m} = 2\delta_{0,m} \tag{3.1.11}$$

Third, the mother wavelet $\phi(t)$ must have vanishing moments

$$\int_{-\infty}^{\infty} \phi(t)t^p dt = 0, \quad p = 0, 1 \tag{3.1.12}$$

This implies that

$$\sum_{k=-\infty}^{\infty} a_k k^p = 0, \quad p = 0, 1 \tag{3.1.13}$$

For the *Daubechies* four-coefficient scaling function, $Eqs(3.1.9), (3.1.11)$ and (3.1.13) yield:

$$\begin{aligned} a_0 + a_1 + a_2 + a_3 &= 2 \\ a_0^2 + a_1^2 + a_2^2 + a_3^2 &= 2 \\ a_0 - a_1 + a_2 - a_3 &= 0 \\ -a_1 + 2a_2 - 3a_3 &= 0 \end{aligned} \tag{3.1.14}$$

Thus, the coefficients a_k for the *Daubechies* scaling function are calculated as

$$\begin{aligned} a_0 &= \frac{1+\sqrt{3}}{4}, \qquad a_1 = \frac{3+\sqrt{3}}{4} \\ a_2 &= \frac{3-\sqrt{3}}{4}, \qquad a_3 = \frac{1-\sqrt{3}}{4} \end{aligned} \tag{3.1.15}$$

3.2. Spatial Discretization

The coupled electric and magnetic fields shown in $Fig(2.1)$ are always perpendicular to each other and there is a half phase difference $\frac{\lambda}{2}$ between them. In order to capture and preserve the self-consistent configuration of the electromagnetic field, a staggered grid

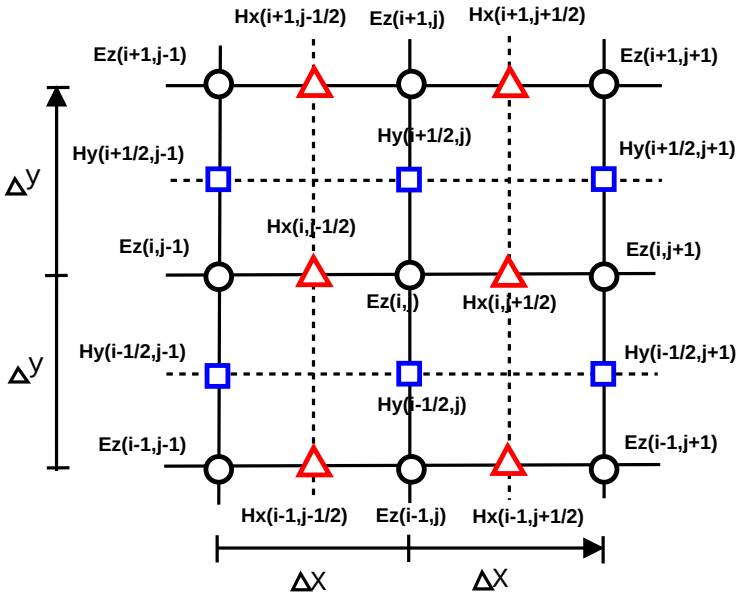

FIGURE 3.3. Electromagnetic Field in Two Dimensions. E_z: Black circle; H_x: Red triangle; H_y: Blue square.

[**2**] is adopted for spatial discretization. As illustrated in $Fig(3.3)$, every E component (circle) is surrounded by two H_x components (triangle) and two H_y components (square) which enables us to evaluate the change of electric field with respect to time $\frac{\partial E}{\partial t}$ at each grid point. This treatment provides a perfect picture of two-dimensional electromagnetic wave propagation being described by *Faraday's Law* and *Ampere's Law*. A staggered grid shown in $Fig(3.3)$ is employed for spatial discretization, where i and j are the row and column indices, respectively. The spatial increment from i to $i+1$ is Δy and from j to $j+1$ is Δx. Let us consider the electric field component $E^z_{i,j}$ under this setting. The first time derivatives of $E^z_{i,j}$ can be evaluated by using central finite difference scheme as:

$$\frac{\partial E^z_{i,j}}{\partial t} = \frac{H^x_{i,j+1/2} - H^x_{i,j-1/2}}{\Delta x} - \frac{H^y_{i+1/2,j} - H^y_{i+1/2,j}}{\Delta y} \tag{3.2.1}$$

In the MRTD analysis, basis functions can be chosen as scaling functions only or both scaling and wavelet functions. To illustrate the proposed boundary procedure, we concern

TABLE 1. Coefficients for the CDF-MRTD scheme [**11**].

	CDF(2,2)	CDF(2,4)	CDF(2,6)
$c(1)$	1.2291666667	1.2918129281	1.3110340773
$c(2)$	-0.0937500000	-0.1371343465	-0.1560100710
$c(3)$	0.0104166667	0.0287617723	0.0419957460
$c(4)$		-0.0034701413	-0.0086543236
$c(5)$		0.0000080265	0.0008308695
$c(6)$			0.0000108999
$c(7)$			-0.0000000041

ourselves with the S-MRTD schemes, i.e., using scaling functions only

$$E_z(x,y,t) = \sum_{i,j=-\infty}^{\infty} E^z_{i,j}(t)\phi_i(x)\phi_j(y) \tag{3.2.2}$$

$$H_x(x,y,t) = \sum_{i,j=-\infty}^{\infty} H^x_{i,j+\frac{1}{2}}(t)\phi_i(x)\phi_{j+\frac{1}{2}}(y) \tag{3.2.3}$$

$$H_y(x,y,t) = \sum_{i,j=-\infty}^{\infty} H^y_{i+\frac{1}{2},j}(t)\phi_{i+\frac{1}{2}}(x)\phi_j(y) \tag{3.2.4}$$

where ϕ is an appropriate scaling function for the particular scheme being used, and the unknown field expansion coefficients $E^z_{i,j}(t)$, $H^x_{i,j+\frac{1}{2}}(t)$, and $H^y_{i+\frac{1}{2},j}(t)$ are time dependent. Here the function ϕ is the scaling function

$$\phi_k(m) = (\frac{m}{\Delta m} - k), \qquad for \quad m = x, y \quad and \quad \Delta m = \Delta x, \Delta y$$

Evaluate the integrals (3.2.5)-(3.2.8). The coefficients $c(l)$ are shown in Table1.

$$\int_{-\infty}^{\infty} \phi_i(x)\phi_j(x)dx = \delta_{i,j}\Delta x \tag{3.2.5}$$

$$\int_{-\infty}^{\infty} \phi_i(x)\frac{\partial \phi_{j+\frac{1}{2}}(x)}{\partial x}dx = \sum_{l=-\infty}^{\infty} c(l)\delta_{i+l,j} \tag{3.2.6}$$

$$\int_{-\infty}^{\infty} \phi_i(y)\phi_j(y)dy = \delta_{i,j}\Delta y \tag{3.2.7}$$

$$\int_{-\infty}^{\infty} \phi_i(y)\frac{\partial \phi_{j+\frac{1}{2}}(y)}{\partial y}dy = \sum_{l=-\infty}^{\infty} c(l)\delta_{i+l,j} \tag{3.2.8}$$

In a homogeneous medium, the MRTD semi-discretization of Maxwell's equations $Eqs(2.3.1)$ can be given as

$$\frac{\partial E^z_{i,j}(t)}{\partial t} = \sum_m \frac{c(l)}{\epsilon \Delta x}\Big(H^y_{i+m-\frac{1}{2},j}(t) - H^y_{i-m+\frac{1}{2},j}(t)\Big) - \sum_m \frac{c(l)}{\epsilon \Delta y}\Big(H^x_{i,j+m-\frac{1}{2}}(t) - H^x_{i,j-m+\frac{1}{2}}(t)\Big) \tag{3.2.9}$$

$$\frac{\partial H^x_{i,j+\frac{1}{2}}(t)}{\partial t} = -\sum_m \frac{c(l)}{\mu \Delta y}\Big(E^z_{i,j+m}(t) - E^z_{i,j-m+1}(t)\Big) \tag{3.2.10}$$

$$\frac{\partial H^y_{i+\frac{1}{2},j}(t)}{\partial t} = \sum_m \frac{c(l)}{\mu \Delta x}\Big(E^z_{i+m,j}(t) - E^z_{i-m+1,j}(t)\Big) \tag{3.2.11}$$

In the present MRTD calculations, the Cohen-Daubechies-Feauveau (CDF) MRTD coefficients [**11**] will be employed for $c(l)$ and are given in the $Table(1)$. For such MRTD methods, the spatial order of accuracy of the CDF$(2,n)$ biorthogonal family is known to be $2+n$ [**12**]. Thus, the order of accuracy in space for the CDF(2,2), CDF(2,4), and CDF(2,6) MRTD schemes is, respectively, four, six, and eight. The temporal discretization of $Eq(3.2.9) - Eq(3.2.11)$ can be simply formulated by using various standard time stepping methods. Consider the vector form of the semi-discretizations $Eq(3.2.9) - Eq(3.2.11)$

$$\frac{\partial \mathbf{U}}{\partial t} = f(\mathbf{U}, t), \tag{3.2.12}$$

where $\mathbf{U}$ contains discrete values of the three field components E_z, H_x and H_y. The classical fourth order Runge-Kutta method will be utilized to update solution $\mathbf{U}^n$ to $\mathbf{U}^{n+1}$:

$$\begin{aligned}
\mathbf{U}^{n+1} &= \mathbf{U}^n + \frac{\Delta t}{6}(K_1 + 2K_2 + 2K_3 + K_4) \\
K_1 &= f(\mathbf{U}^n, t_n) \\
K_2 &= f(\mathbf{U}^n + \frac{1}{2}\Delta t K_1, t_{n+\frac{1}{2}}) \\
K_3 &= f(\mathbf{U}^n + \frac{1}{2}\Delta t K_2, t_{n+\frac{1}{2}}) \\
K_4 &= f(\mathbf{U}^n + \Delta t K_3, t_{n+1})
\end{aligned} \tag{3.2.13}$$

where $\mathbf{U}^n$ is the solution at time $t_n = n\Delta t$ and Δt is the time increment. Therefore, both spatial and temporal orders of accuracy are at least four for the present MRTD analysis. However, the overall high order of accuracy of the present MRTD approach can still be impaired by deficient treatments of boundary conditions, particularly when complicated boundary conditions are encountered.

3.3. Image principle

In the MRTD methods, the image principle is commonly used to deal with the PEC and PMC boundary conditions. This is a treatment to implement simple boundary conditions by assuming that there is a one-to-one correspondence between the inner grid node and the imaging fictitious node outside the domain (near the boundary). For example, consider a uniform grid $x_{-M} < \cdots < a = x_0 < x_1 < \cdots < x_N = b < \cdots < x_{N+M}$. Here the actual mesh size of the x partition is $N + 1$, while M represents the maximal number of fictitious points needed in a particular MRTD scheme, in order to ensure the MRTD spatial approximations $Eq(3.2.9) - Eq(3.2.11)$ throughout the domain $[a, b]$. Consider the right boundary shown in $Fig(3.4)$ as an example and denote a function u to be either E or H. One could assume the following one-to-one image principle at the boundary

$$u(x_{N+j}) - u(x_N) = a_j[u(x_{N-j}) - u(x_N)], \tag{3.3.1}$$

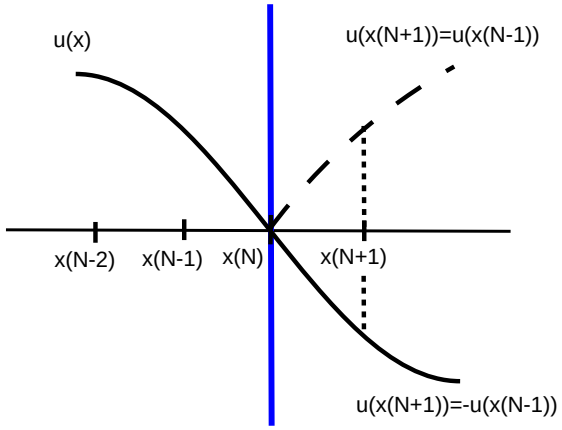

FIGURE 3.4. An illustration of the image principle for a physical boundary has symmetric or antisymmetric property. The blue line represents the physical boundary

for $j = 1, 2, \ldots, M$. In the PEC condition, we have $E_z = 0$ at the right end $x = b$. By using Maxwell's equations, one can further derive that $\frac{\partial^2 E_z}{\partial x^2} = 0$ at $x = b$ [**39**]. Evaluating the second derivative of E_z at x_N, we have:

$$E_z^{(2)}(x_N) = \frac{E_z(x_{N-1}) - 2E_z(x_N) + E_z(x_{N+1})}{(\Delta x)^2}$$

$$0 = E_z(x_{N-1}) - 2E_z(x_N) + E_z(x_{N+1})$$

$$E_z(x_{N+1}) - E_z(x_N) = (-1)\left[E_z(x_{N-1}) - E_z(x_N)\right] \tag{3.3.2}$$

Thus, the PEC condition for E_z can be satisfied by choosing $a_j = -1$ in $Eq(3.3.1)$. This is also called an anti-symmetric boundary extension [**18**]. Similarly, the PEC condition for H_y, i.e., $\frac{\partial H_y}{\partial x} = 0$, can be imposed by taking $a_j = 1$ in $Eq(3.3.1)$. This is also called a symmetric boundary extension [**18**].

The image principle, $Eq(3.3.1)$, can actually handle some boundary conditions that are more complicated than the PEC ones. See the reference [**18**] for more details. However, the image principle has a major limitation when some physical boundaries do not have any symmetric or antisymmetric properties. As we show in $Fig(3.5)$, it is difficult to find a one-to-one correspondence between the inner grid node and the imaging fictitious node outside the domain, especially, when the boundary condition is a function of space or time.

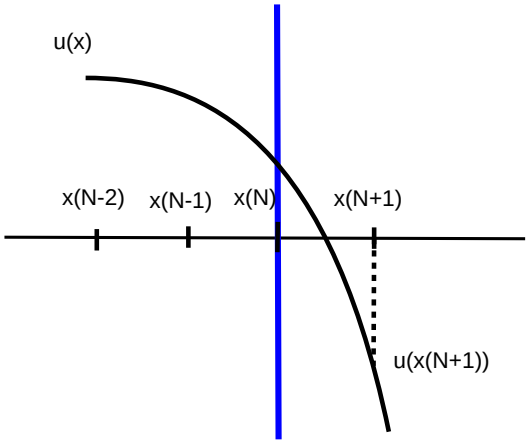

FIGURE 3.5. An illustration of a physical boundary without symmetric or antisymmetric property

Therefore, the derivatives near the boundary are no longer accurate when a central finite difference scheme is applied using fictitious points outside the computational domain.

3.4. Matched interface and boundary (MIB) treatment

For more general boundary conditions, such as the Robin condition, the image principle $Eq(3.3.1)$ cannot be rigorously valid for the reason we have mentioned above. A more reasonable assumption is that a fictitious value $u(x_{N+j})$ should not depend on one inner value $u(x_{N-j})$ only. It should instead depend on *a set of* function values inside the boundary. This motivates the development of the MIB boundary scheme [**17, 18**].

We illustrate the idea by considering a Robin type boundary condition at $x = b$:

$$\frac{\partial u}{\partial x} - ku = \phi(t). \tag{3.4.1}$$

The MIB boundary treatment assumes a function relation which is generalized from the image principle:

$$u(x_{N+j}) = \sum_{i=0}^{L} r_{i,j} u(x_{N-i}) + r_{L+1,j}\phi(t), \tag{3.4.2}$$

where the $r_{i,j}$ are the MIB representation coefficients and $j = 1, 2, \ldots, M$. Thus, in the MIB discretization, each fictitious value outside the domain will depend on $L+1$ inner values and

one inhomogeneous boundary value $\phi(t)$. An iterative procedure is commonly used in the MIB method to determine these fictitious values one by one.

At the first step, since only one boundary condition is available, one can only determine one fictitious point $u(x_{N+1})$, see $Fig(3.6)$. In the MIB scheme, the first derivative in the Robin condition $Eq(3.4.1)$ is approximated by using a one-sided finite difference with $L+1$ grid points inside and one fictitious node outside. In particular, we choose $x = b$ as the differentiation point of the finite difference and denote it as the origin of the local grid stencil: $(-L\Delta x, \ldots, -\Delta x, 0, \Delta x)$. We denote the corresponding finite difference weights to be $(C_{-L}^{(L+2)}, \ldots, C_{-1}^{(L+2)}, C_0^{(L+2)}, C_1^{(L+2)})$. Here the subscript of the weight $C_i^{(L+2)}$ is for the local grid index, while the superscript represents the fact that there are totally $L+2$ nodes in this stencil. Based on such a partition, the boundary condition $Eq(3.4.1)$ is discretized to be

$$\sum_{i=-L}^{1} C_i^{(L+2)} u(x_{N+i}) - k u(x_N) = \phi(t) \tag{3.4.3}$$

The only unknown $u(x_{N+1})$ in $Eq(3.4.3)$ can be solved in terms of the other values, giving rise to the following representation coefficients: $r_{0,1} = (k - C_0^{(L+2)})/C_1^{(L+2)}$, $r_{L+1,1} = 1/C_1^{(L+2)}$, and $r_{i,1} = -C_{-i}^{(L+2)}/C_1^{(L+2)}$ for $i = 1, 2, \ldots, L$.

At the second step, we introduce a second fictitious value $u(x_{N+2})$, see $Fig(3.6)$. One possible way is to solve for $u(x_{N+2})$ in a process similar to that in the first step, by also considering only one fictitious node outside the domain. A more accurate treatment is usually employed in the MIB scheme by considering two fictitious nodes simultaneously. The same boundary condition $Eq(3.4.1)$ is now discretized as

$$\sum_{i=-L}^{2} C_i^{(L+3)} u(x_{N+i}) - k u(x_N) = \phi(t) \tag{3.4.4}$$

where the $C_i^{(L+3)}$ are the finite difference weights to approximate the first derivative at $x = 0$ based on a local grid stencil: $(-L\Delta x, \ldots, -\Delta x, 0, \Delta x, 2\Delta x)$. Here the superscript indicates that there are totally $L+3$ nodes involved in this approximation. From $Eq(3.4.4)$, one can solve $u(x_{N+2})$ in terms of the others. Then, the known representation coefficients

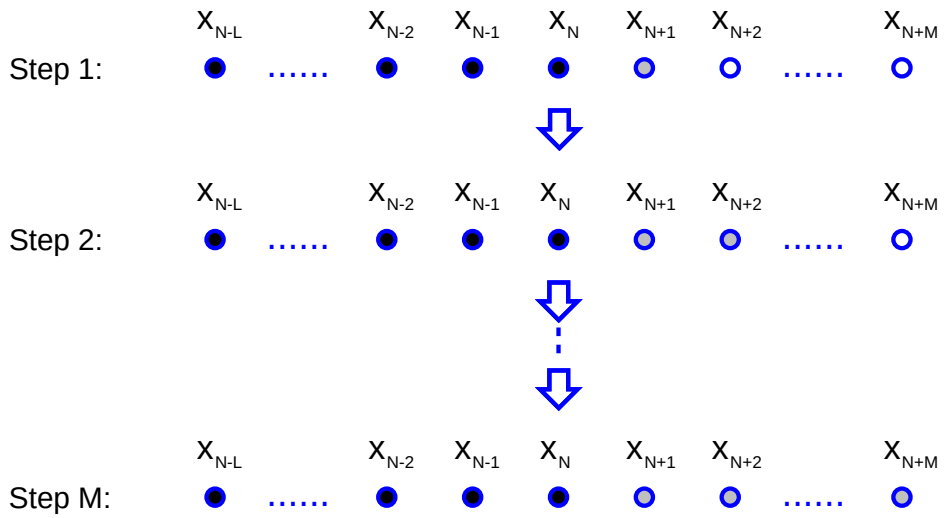

FIGURE 3.6. Illustration of the MIB grid partition and the iterative procedure. Filled circles: regular nodes; Partially filled circles: solved fictitious nodes; Open circles: unsolved fictitious nodes.

for $u(x_{N+1})$ from the first step can be substituted in so that $u(x_{N+2})$ will also depend on $L+1$ regular function values and $\phi(t)$. Consequently, the representation coefficients $r_{i,2}$ for $i = 0, \ldots, L+1$ can be attained. Through such an iterative procedure, all the M fictitious points can be efficiently determined in M steps, as shown in $Fig(3.6)$. The MIB treatment of other boundary conditions can be similarly carried out.

We note that in the MIB method, boundary conditions are enforced systematically so that, in principle it can achieve arbitrarily high orders. In practice, the order of accuracy of the MIB scheme is dominated by the total number of interior support nodes L. One has a certain amount of flexibility in choosing L in the finite difference approximation. A sufficiently large L value is usually selected to ensure that the order of accuracy in the MIB boundary treatment is not less than that of the MRTD scheme. Nevertheless, for unsteady problems, a very large L may render the MIB method unstable. The stability issue of the MIB method has been discussed in [**18**]. To guarantee stability, one should choose L according to the upbounds established in [**18**]. More details are given in Chapter 5.

An advantage of the generalized image principle $Eq(3.4.2)$ is that the representation coefficients $r_{i,j}$ are independent of the boundary data $\phi(t)$. Consequently, they are time

invariant. Thus, the MIB scheme actually needs to be carried out only once at the beginning, even though $\phi(t)$ takes different values at different times. Therefore, the computational overhead introduced by the MIB boundary treatment is negligibly small in real MRTD computations. In summary, the MIB method provides a fictitious domain support so that the MRTD methods can be applied in a translation invariant manner throughout the domain. Furthermore, since the proposed MIB boundary treatment does not depend on the MRTD discretizations, this boundary closure scheme can be applied to other high order FDTD methods.

CHAPTER 4

NUMERICAL DISPERSION ANALYSIS

The MIB-MRTD algorithm for *Maxwell's* equations reviewed in Chapter 3, like other numerical algorithms, causes nonphysical dispersion of the simulated waves in a free-space computational domain. That is, the phase velocity of the numerical wave modes can differ from the real phase velocity by an amount varying with the wavelength, direction of propagation in the grid, and grid discretization. It is necessary for us to conduct a numerical dispersion analysis and compare with some existing numerical algorithms in order to make further improvements in terms of accuracy, stability and computational cost.

4.1. One Dimensional Scalar Wave Equation

We begin our discussion of numerical dispersion with the classical one dimensional scalar wave equation

$$\frac{\partial^2 u}{\partial t^2} = c^2 \frac{\partial^2 u}{\partial x^2} \tag{4.1.1}$$

where $u = u(x,t)$. Here c is a positive constant that has the physical interpretation of wave speed. A general solution of $Eq(4.1.1)$ can be constructed as

$$u(x,t) = F(x+ct) + G(x-ct) \tag{4.1.2}$$

where F and G are functions of one variable determined by appropriate initial conditions:

$$u(x,0) = u_0(x), \quad u_t(x,0) = u_1(x) \tag{4.1.3}$$

We are able to solve $Eq(4.1.1)$ as

$$u(x,0) = F(x) + G(x) = u_0(x)$$
$$u_t(x,0) = cF'(x) - cG'(x) = u_1(x) \tag{4.1.4}$$

The second equation gives

$$F(x) = G(x) + \frac{1}{c}\int_0^x u_1(s)ds + L \tag{4.1.5}$$

So we have

$$F(x) + G(x) = u_0(x)$$
$$F(x) - G(x) = \frac{1}{c}\int_0^x u_1(s)ds + L \tag{4.1.6}$$

It follows that

$$F(x) = \frac{1}{2}u_0(x) + \frac{1}{2c}\int_0^x u_1(s)ds + \frac{L}{2}$$
$$G(x) = \frac{1}{2}u_0(x) - \frac{1}{2c}\int_0^x u_1(s)ds - \frac{L}{2} \tag{4.1.7}$$

Therefore, we obtain the solution of $Eq(4.1.1)$ as

$$u(x,t) = \frac{[u_0(x+ct) + u_0(x-ct)]}{2} + \frac{1}{2c}\int_{x-ct}^{x+ct} u_1(s)ds \tag{4.1.8}$$

which is known as *D'Alembert's* formula [**34**].

4.2. The Dispersion Relation for The One-Dimensional Wave Equation

Dispersion is defined as the variation of a propagating wave's wavelength λ with frequency f . Conventionally, dispersion is also represented as the variation of the propagating wavenumber $k = 2\pi/\lambda$ with angular frequency $\omega = 2\pi f$. Consider a continuous

sinusoidal-traveling-wave function [**35**]:

$$u(x,t) = e^{i(\omega t - kx)} \tag{4.2.1}$$

where ω and k are defined above and $i = \sqrt{-1}$. Substituting into $Eq(4.2.1)$, we obtain

$$(i\omega)^2 e^{i(\omega t - kx)} = c^2(-ik)^2 e^{i(\omega t - kx)} \tag{4.2.2}$$

Canceling the exponential terms on both sides of the equation yields

$$\omega^2 = c^2 k^2 \tag{4.2.3}$$

$Eq(4.3.7)$ is the dispersion relation for the one-dimensional scalar wave equation. This simple relation states that the wavenumber is linearly proportional to the sinusoidal frequency. The plus sign designates $+x$-directed wave propagation, while the minus sigh designates $-x$-directed propagation. Further, an expression for the phase velocity can be simply derived from $Eq(4.3.7)$ as:

$$v_p = \frac{\omega}{k} = \pm c \tag{4.2.4}$$

4.3. Numerical Dispersion Relation

Let us start our discussion of the numerical dispersion relation from the classical finite-difference approximation. Consider the sinusoidal wave given by $Eq(4.2.1)$ of angular frequency ω discretized in space and time at (x_m, t_n). Let $\tilde{k} = \tilde{k}_{real} + i\tilde{k}_{imag}$ be the possible complex-valued wavenumber of this "numerical" wave. Then we have

$$\begin{aligned} u_m^n = e^{i(\omega n\Delta t - \tilde{k} m\Delta x)} &= e^{i\left[\omega n\Delta t - (\tilde{k}_{real} + i\tilde{k}_{imag})\right] m\Delta x} \\ &= e^{\tilde{k}_{imag} m\Delta x} e^{i(\omega n\Delta t - \tilde{k}_{real} m\Delta x)} \end{aligned} \tag{4.3.1}$$

where Δx and Δt are the spatial and temporal increments. In general, $\tilde{k}$ differs from k, the corresponding physical wavenumber. This difference, called the numerical-dispersion artifact, may give rise to numerical wave amplitudes and velocities that depart from the

exact values. Now we apply the standard central finite difference method to solve for u_m^{n+1}. $Eq(4.1.1)$ (see appendix A for more details) yields:

$$u_m^{n+1} = \left(\frac{c\Delta t}{\Delta x}\right)^2 \left\{u_{m+1}^n - 2u_m^n + u_{m-1}^n\right\} + 2u_m^n - u_m^{n-1} \tag{4.3.2}$$

substitute u_m^n defined in $Eq(4.3.1)$, we obtain:

$$\begin{aligned} e^{i\left[\omega(n+1)\Delta t - \tilde{k}m\Delta x\right]} = \left(\frac{c\Delta t}{\Delta x}\right)^2 \{e^{i\left[\omega n\Delta t - \tilde{k}(m+1)\Delta x\right]} - 2e^{i\left[\omega n\Delta t - \tilde{k}m\Delta x\right]} \\ + e^{i\left[\omega n\Delta t - \tilde{k}(m-1)\Delta x\right]}\} + 2e^{i\left[\omega n\Delta t - \tilde{k}m\Delta x\right]} - e^{i\left[\omega(n-1)\Delta t - \tilde{k}m\Delta x\right]} \end{aligned} \tag{4.3.3}$$

By canceling $e^{i(\omega n\Delta t - \tilde{k}m\Delta x)}$, we obtain

$$e^{i\omega\Delta t} = \left(\frac{c\Delta t}{\Delta x}\right)^2 \left(e^{-i\tilde{k}\Delta x} - 2 + e^{i\tilde{k}\Delta x}\right) + 2 - e^{-i\omega\Delta t} \tag{4.3.4}$$

Grouping the time and space exponential terms yields

$$\frac{e^{i\omega\Delta t} + e^{-i\omega\Delta t}}{2} = \left(\frac{c\Delta t}{\Delta x}\right)^2 \left(\frac{e^{-i\tilde{k}\Delta x} + e^{i\tilde{k}\Delta x}}{2} - 1\right) + 1 \tag{4.3.5}$$

A simple application of *Euler's* identity to the complex exponentials, yields the numerical dispersion relation

$$\cos(\omega\Delta t) = \left(\frac{c\Delta t}{\Delta x}\right)^2 \left[cos(\tilde{k}\Delta x) - 1\right] + 1 \tag{4.3.6}$$

$$\tilde{k} = \frac{1}{\Delta x} cos^{-1} \left\{1 + \left(\frac{c\Delta t}{\Delta x}\right)^2 [\cos(\omega\Delta t) - 1]\right\} \tag{4.3.7}$$

This can be simplified using the half angle formula:

$$\left[\frac{1}{c\Delta t}\sin\left(\frac{\omega\Delta t}{2}\right)\right]^2 = \left[\frac{1}{\Delta x}\sin\left(\frac{\tilde{k}\Delta x}{2}\right)\right]^2 \tag{4.3.8}$$

Consider a choice of space and time increments such that $\frac{c\Delta t}{\Delta x} = \frac{1}{4}$ and let $c = 1$, $\Delta x = \frac{\lambda_0}{5}$, where λ_0 is the free-space wavelength of a continuous propagating wave of angular frequency

ω. From $Eq(4.3.7)$, we have

$$\begin{aligned}\tilde{k} &= \frac{1}{\Delta x}\cos^{-1}\left\{1+\left(\frac{\Delta x}{\Delta x/4}\right)^2\left[\cos\left(\frac{\omega\Delta x}{4}\right)-1\right]\right\} \\ &= \frac{1}{\Delta x}\cos^{-1}\left\{1+16\left[\cos\left(\frac{k\Delta x}{4}\right)-1\right]\right\} \end{aligned} \tag{4.3.9}$$

Since $k=\frac{\omega}{c}=\frac{2\pi}{\lambda_0}$, we obtain:

$$\begin{aligned}\tilde{k} &= \frac{1}{\Delta x}\cos^{-1}\left\{1+16\left[\cos\left(\frac{2\pi}{\lambda_0}\cdot\frac{\Delta x}{2}\right)-1\right]\right\} \\ &= \frac{1}{\Delta x}\cos^{-1}(0.2169) \\ &= \frac{1.3522}{\Delta x} \end{aligned} \tag{4.3.10}$$

Defining a numerical phase velocity $\tilde{v}_p$ by analogy to the phase velocity for the continuous wave equation, $Eq(4.1.1)$,

$$\tilde{v}_p = \frac{\omega}{\tilde{k}} \tag{4.3.11}$$

we have

$$\tilde{v}_p = \frac{2\pi f}{1.3522/\Delta x} = \frac{2\pi(c/\lambda_0)\Delta x}{1.3522} = \frac{2\pi(0.2)}{1.3522}c = 0.9294c \tag{4.3.12}$$

The numerical phase velocity for this example is seen to be 7.06% less than the free-space phase velocity c, which is considerably large. In a similar manner, we can derive the general numerical dispersion relation for *Yee's* finite-difference algorithm [**2**] in three dimension is given as

$$\begin{aligned}\left[\frac{1}{c\Delta t}\sin\left(\frac{\omega\Delta t}{2}\right)\right]^2 = &\left[\frac{1}{\Delta x}\sin\left(\frac{\tilde{k}_x\Delta x}{2}\right)\right]^2+\left[\frac{1}{\Delta y}\sin\left(\frac{\tilde{k}_y\Delta y}{2}\right)\right]^2 \\ &+\left[\frac{1}{\Delta z}\sin\left(\frac{\tilde{k}_z\Delta z}{2}\right)\right]^2 \end{aligned} \tag{4.3.13}$$

Such a numerical result is hard to be accepted as a good approximation of the propagating wave. Thus, we have to either refine our mesh grid or look for other low dispersive error methods to improve the accuracy. The numerical dispersion relation for S-MRTD [**41**] in

three dimensions is formulated as

$$\left[\frac{1}{c\Delta t}\sin\left(\frac{\omega\Delta t}{2}\right)\right]^2 = \left[\frac{1}{\Delta x}\sum_l a(l)\sin\left(\frac{\tilde{k}_x\Delta x}{2}(l+\frac{1}{2})\right)\right]^2 + \left[\frac{1}{\Delta y}\sum_l a(l)\sin\left(\frac{\tilde{k}_y\Delta y}{2}(l+\frac{1}{2})\right)\right]^2 + \left[\frac{1}{\Delta z}\sum_l a(l)\sin\left(\frac{\tilde{k}_z\Delta z}{2}(l+\frac{1}{2})\right)\right]^2 \tag{4.3.14}$$

where the $a(l)$ here are the MRTD discretization coefficients in $Table(1)$. However, it is laborious to derive an analytic numerical dispersion relation formula for our proposed method due to the MIB process. Therefore, we will focus on the numerical results in the frequency space.

4.4. A Fourier Analysis of The Computational Errors

The dispersion error can be analyzed by using *Fourier* transform for wave conversion from physical space to frequency space [**16**].

$$\mathcal{F}[u(x)] = \frac{1}{2\pi}\int_{-\infty}^{\infty} u(x)e^{ikx}dx \tag{4.4.1}$$

Here $i = \sqrt{-1}$. The *Fourier* transform of the n^{th} derivative is given by

$$\mathcal{F}[u^{(n)}(x)] = (ik)^n\mathcal{F}[u(x)] \tag{4.4.2}$$

This leads to

$$\mathcal{F}\left[\frac{du}{dx}\right] = ik\mathcal{F}[u(x)] \tag{4.4.3}$$

for $n = 1$. By the convolution theorem, the corresponding *Fourier* coefficients of the derivatives satisfy

$$\mathcal{F}[\delta^{(n)}_{h,M}(x) * u(x)] = \mathcal{F}[\delta^{(n)}_{h,M}(x)]\mathcal{F}[u(x)] \tag{4.4.4}$$

where $*$ denotes the convolution and $\delta^{(n)}_{h,M}$ is the kernel of the numerical algorithm to be investigated. Here, the subscripts h and M represent the spatial increment and the number

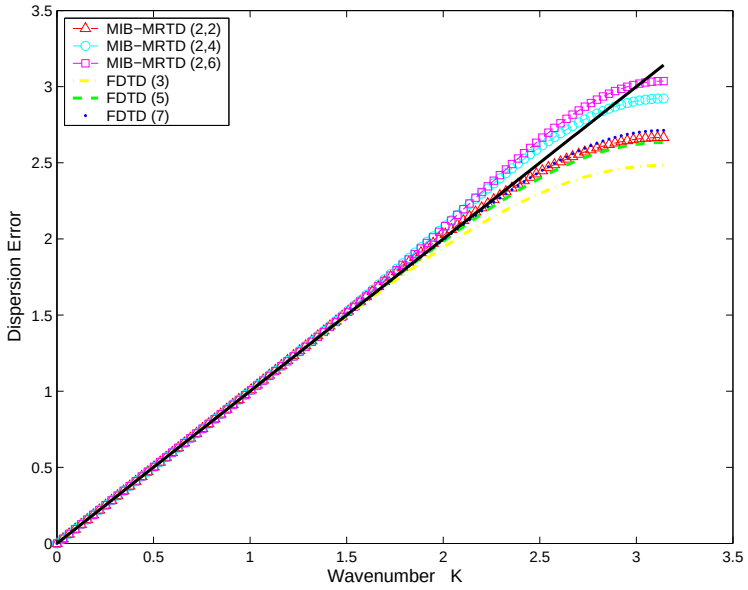

FIGURE 4.1. Numerical Dispersion Error at Different Frequencies

of points using in the kernel. The terms on the left-hand side of the $Eq(4.4.3)$ and $Eq(4.4.4)$ all represent the first derivative of $u(x)$. Thus, we have:

$$\begin{aligned} ik\mathcal{F}[u(x)] &= \mathcal{F}[\delta^{(1)}_{h,M}]\mathcal{F}[u(x)] \\ ik &= \mathcal{F}[\delta^{(1)}_{h,M}] \\ k &= -i\mathcal{F}[\delta^{(1)}_{h,M}] \end{aligned} \tag{4.4.5}$$

Denote k^* as an approximation the of the physical wavenumber k, thus $k^* = -i\mathcal{F}[\delta^{(1)}_{h,M}]$. Introduce a scaled wavenumber $\omega^* = hk^*$ and $\omega = hk$. For simplicity and without loss of generality, we let h=1, so that the dispersive error of the given algorithm can be measured by the difference between ω^* and ω within the domain of the wavenumber $w \in [-\pi, \pi]$. From $Fig(4.1)$, we see that the high-order finite difference method can provide very good approximations when the frequency is relatively low, however the dispersion error increases dramatically when ω is large. On the other hand, the MIB-MRTD method is able to maintain low dispersion error over a broader frequency band.

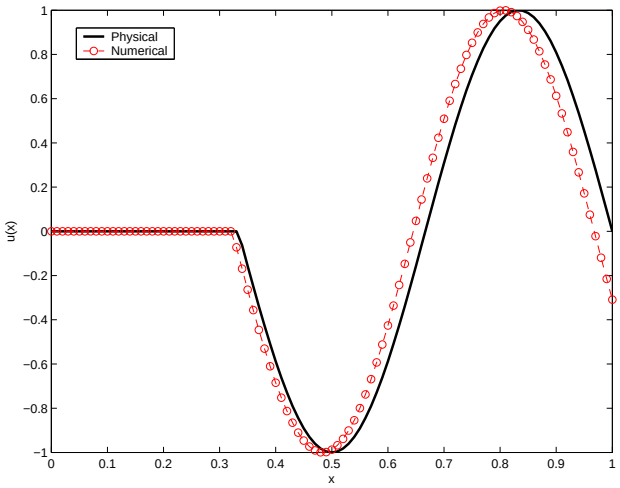

FIGURE 4.2. Numerical Dispersion Error

4.5. An Example: The One-Way Wave Equation

The prototype for all hyperbolic partial differential equations is the one-way wave equation:

$$\frac{\partial u}{\partial t} = c\frac{\partial u}{\partial x} \tag{4.5.1}$$

where c is a constant representing the wave speed. Given the initial and boundary conditions:

$$\begin{aligned} &u(x,0) = \sin(3\pi x) \\ &u(0,t) = \sin(3\pi t), \quad u(1,t) = sin(3\pi(1+t)) \end{aligned} \tag{4.5.2}$$

it is not difficult to obtain the analytic solution $u(x,t) = \sin(3\pi(x+t)), \quad 0 \le x \le 1, t \ge 0$. As was discussed before, because of the existence of numerical dispersion, the accumulated discrepancies between the "computed wave" and the physical wave will become very noticeable after a certain amount of time. The solution of $Eq(4.5.1)$ is a sinusoidal function with $\lambda = \frac{2}{3}$, but we only focus on the dispersion error between a single period in $Fig(4.2)$. If we take a close look along the time axis in $Fig(4.3)$, we will see that the wave propagation is actually a horizontal shifting of the original wave over time.

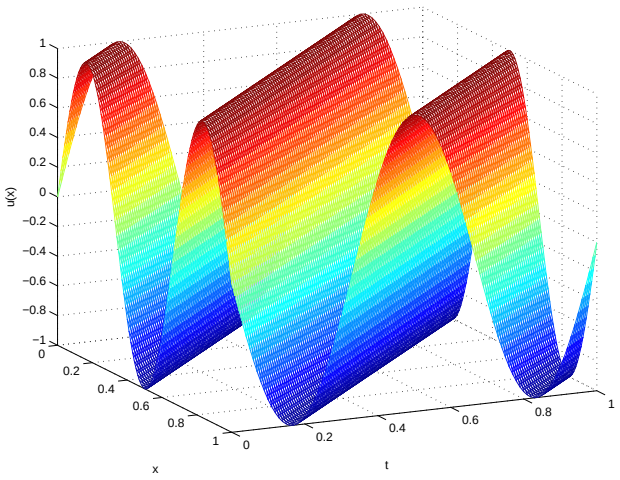

FIGURE 4.3. One-Way Wave Equation

CHAPTER 5

NUMERICAL STABILITY ANALYSIS

Numerical stability analysis is indispensable for a given numerical algorithm in terms of the optimized choices of space and time increments, numerical efficiency and effectiveness. In this chapter, we will analyze the numerical stability of the MIB-MRTD method from a matrix structure angle.

5.1. Discretization Matrix

The Runge-Kutta method we use as our time integrator can be written in a compact matrix form:

$$\frac{d}{dt}U = AU \tag{5.1.1}$$

where A is the MIB-MRTD spatial discretization matrix. In other words, we multiply the matrix A to get spatial derivatives of U on each grid point. Therefore, the matrix A is in composition of the MRTD kernels we have seen in chapter 3 across its diagonal lines. In $Fig(5.1)$, we give two examples of MIB-MRTD matrices, where in both cases $M = 7$. In case (a), we use $L = M$ inner points for fictitious points extension, so that the MIB process does not refer to any point outside the computational stencil. It can be seen that in $Fig(5.1.a)$, the M fictitious points in the first row can be linearly represented by the first seven inner points. In the next row, the $M-1$ fictitious points also depend on the first seven inner points. The eighth inner point does not involve in the MIB process and will inherit the last coefficient from the MRTD kernel. The number of the inner points called by matrix A increase by one at each step before it reach the full stencil length $2S$. In case (b), we use $L = 2M$ inner points for a fictitious points extension. Thus the M fictitious points in the first row totally depend on the first fourteen inner points. That is reason why the number of the inner points called by matrix A stay the same on each row in case (b).

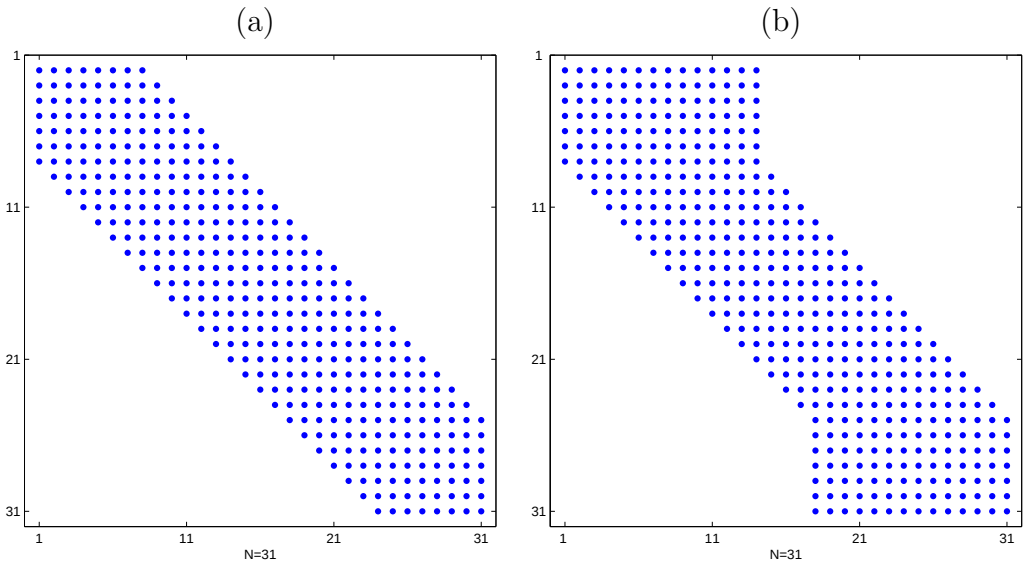

FIGURE 5.1. Discretization Matrix of The MIB-MRTD Method. (a) M=7, L=7; (b) M=7, L=14.

Let us reconsider the hyperbolic $Eq(4.1.1)$

$$\frac{\partial^2 u}{\partial t^2} = c^2 \frac{\partial^2 u}{\partial x^2}$$

We can not simply use Runge-Kutta method to solve $Eq(4.1.1)$, because the term on the left side involves the second order derivative with respect to time. Instead, we can solve a system of differential equations $Eq(2.4.1)$ to overcome this difficulty.

$$\mu \frac{\partial H_y}{\partial t} = \frac{\partial E_z}{\partial x}$$
$$\epsilon \frac{\partial E_z}{\partial t} = \frac{\partial H_y}{\partial x}$$

to show the equivalency, we take the partial space derivative of $Eq(2.4.1)$,

$$\frac{\partial}{\partial t}\left(\frac{\partial E_z}{\partial t} = \frac{1}{\epsilon}\cdot\frac{\partial H_y}{\partial x}\right) \quad \rightarrow \quad \frac{\partial^2 E_z}{\partial t^2} = \frac{1}{\epsilon}\cdot\frac{\partial^2 H_y}{\partial t \partial x} \tag{5.1.2}$$

$$\frac{\partial}{\partial x}\left(\frac{\partial H_y}{\partial t} = \frac{1}{\mu}\cdot\frac{\partial E_z}{\partial x}\right) \quad \rightarrow \quad \frac{\partial^2 H_y}{\partial x \partial t} = \frac{1}{\mu}\cdot\frac{\partial^2 E_z}{\partial x^2} \tag{5.1.3}$$

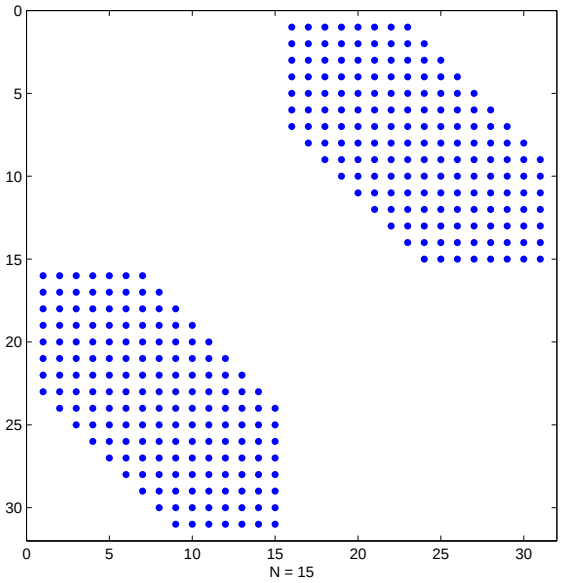

FIGURE 5.2. Dicretization Matrix for One-Dimensional Wave Equation

Upon substituting the $\frac{\partial^2 H_y}{\partial x \partial t}$ in $Eq(5.1.3)$ into the $\frac{\partial^2 H_y}{\partial t \partial x}$ in $Eq(5.1.2)$, we obtain

$$\frac{\partial^2 E_z}{\partial t^2} = \frac{1}{\epsilon\mu} \cdot \frac{\partial^2 E_z}{\partial x^2} = c^2 \frac{\partial^2 E_z}{\partial x^2} \tag{5.1.4}$$

where $c = 1/\sqrt{\mu\epsilon}$. Equation (5.1.4) is a one-dimensional scalar wave equation for E_z, which plays the role of u in $Eq(4.1.1)$.

The one-dimensional *Maxwell's* equations in matrix form is

$$\frac{\partial}{\partial t} \begin{pmatrix} E_z \\ H_y \end{pmatrix} = \begin{pmatrix} 0 & \frac{1}{\epsilon}\frac{\partial}{\partial x} \\ \frac{1}{\mu}\frac{\partial}{\partial x} & 0 \end{pmatrix} \begin{pmatrix} E_z \\ H_y \end{pmatrix}$$

The corresponding discretization matrix is shown in $Fig(5.2)$. This matrix is composed of two diagonal matrices we show in $Fig(5.1)$, where $M = 7, L = 7$ and $N = 15$ in this case. We note that although the boundary conditions may or may not be time-dependent, the MIB-MRTD representation coefficients of fictitious points actually only need to be calculated once to construct A. The constant matrix A can be used at all time steps. To ensure the convergency of the MIB-MRTD method, the eigenvalues of A must satisfy certain requirements imposed by the Runge-Kutta method.

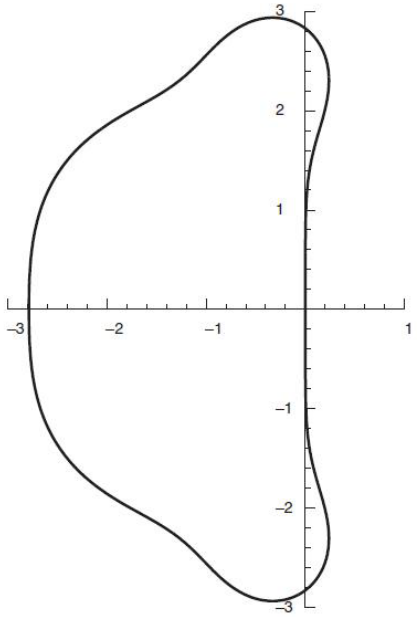

FIGURE 5.3. Stable Region of Runge-Kutta Method

Let us first consider the stable region of RK4. Denoting the eigenvalues of A as λ_i, the RK4 converges if and only if the following relation is satisfied:

$$|S(\Delta t, \lambda_i)| = \left|1 + \Delta t\lambda_i + \frac{(\Delta t\lambda_i)^2}{2!} + \frac{(\Delta t\lambda_i)^3}{3!} + \frac{(\Delta t\lambda_i)^4}{4!}\right| \leq 1 \tag{5.1.5}$$

It is not difficult for us to use *Matlab* or other computer sofewares to plot the stable region shown in $Fig(5.3)$. We notice that for the MIB-MRTD method to converge, the product of $\Delta t \cdot \lambda_i$ has to stay within the stable region. All λ_i can be calculated as long as the the matrix A is determined. So we are able to optimize the choice of Δt in order to reduce computational cost without a compromise of accuracy.

5.2. Courant - Friedrichs - Levy (CFL) Number

Before the quantification of eigenvalues, we will introduce the Courant-Friedrichs -Levy (CFL) number which is a critical measurement for numerical stability and computational effectiveness. The CFL number is defined as the ratio of time increment to space increment $\frac{\Delta t}{\Delta x}$. A larger CFL number implies a more robust numerical algorithm in terms

of better stability and lower computational cost. Let us review the finite different method we discussed in previous chapters. The eigenvalues of the matrix A generated by the finite-difference method in $Eq(4.5.1)$ can be calculated analytically. The *Fourier* modes $e^{i\omega x}$ for the wavenumber ω in the range $\frac{-\pi}{\Delta x} \leq \omega \leq \frac{\pi}{\Delta x}$ with Δx being the spacing. For the central FD approximation to $\frac{\partial}{\partial x}$ with $M = 1$ (second-order central FD), the eigenvalues of A can be found to be

$$Ae^{i\omega x} = \frac{e^{i\omega(x+\Delta x)} - e^{i\omega(x-\Delta x)}}{2\Delta x} = i\frac{sin(\omega\Delta x)}{\Delta x}e^{i\omega x} \tag{5.2.1}$$

Similarly, we can find eigenvalues of A for the $2M^{th}$ order central approximation as

$$Ae^{i\omega x} = i\frac{\sin\omega\Delta x}{\Delta x}\sum_{k=0}^{M-1}\frac{(k!)^2}{(2k+1)!}2^{2k}\left(\sin\frac{\omega\Delta x}{2}\right)^{2k}e^{i\omega x} \tag{5.2.2}$$

It is not difficult to see from $Eq(5.2.1)$ that the eigenvalues of the central FD approximation to the first derivatives are all purely imaginary numbers. From the stable region shown in $Fig(5.3)$, along the imaginary axis, the RK4 will be stable within the interval $(-2\sqrt{2}i, 2\sqrt{2}i)$. Here, we denote λ as the spectral radius of the central FD matrix A, i.e.$\lambda = max_{0\leq i\leq N}|\lambda_i|$. We then find that the central FD method will be stable if $|\lambda\Delta t| \leq 2\sqrt{2}$. For the central FD with $M = 1$, one can derive from $Eq(5.2.1)$ that $\lambda = \frac{1}{\Delta x}$. Thus, the second-order central FD is stable if $\Delta t \leq 2\sqrt{2}\Delta x$. In other words, the corresponding CFL number is $2\sqrt{2}$. Now, let us return to the eigenvalues of MIB-MRTD matrices. $Fig(5.4)$ shows distributions of eigenvalues of the matrix in $Fig(5.2)$. We notice that all eigenvalues of the MIB-MRTD matrix are located along the complex axis which is a desirable result for stability consideration. Compared with the stable region shown in $Fig(5.3)$, the RK4 method will be unconditionally unstable if some of the eigenvalues are located on the right half part of the complex plane. In other words, the RK4 method will converge if and only if $\lambda \cdot \Delta t \leq 0$, indicating $\Delta t \to 0$ which is computationally impossible.

We investigate the stabilities of the MIB-FDTD and MIB-MRTD methods by considering two theoretical features of the discrete spectrum of A. First, in comparing with

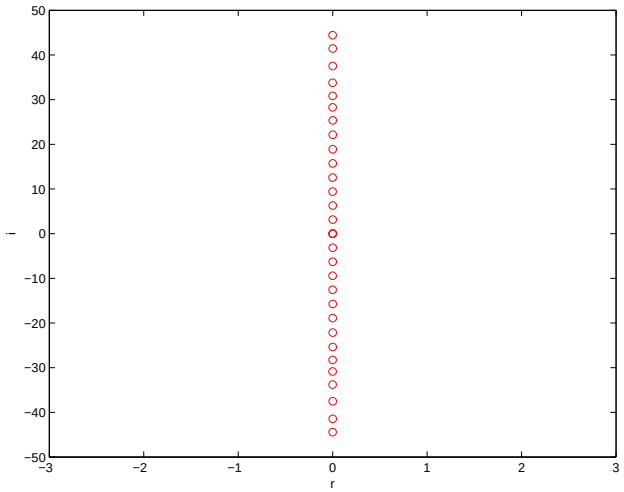

FIGURE 5.4. Eigenvalues of MIB-MRTD Discretization Matrix

the FDTD method with the same M value, the MIB-MRTD matrix might have a different spectral radius λ. Second, due to the anti-symmetry property of A, all of the associated eigenvalues must be complex. However, the MIB method could yield spurious modes when L is large. In the present study, we show that numerical stability could be affected significantly by both spectral radius and spurious modes.

The numerical results are presented in $Table(1)$. It is found that for both MIB-FDTD and MIB-MRTD methods with the same M value, the spectral radius λ is not affected by L. Moreover, we notice that there exists a critical upper bound $L^* = 7$, for different M values, the FDTD and MIB-MRTD methods are stable if $L \leq L^*$. Two significant conclusions can be drawn based on the numerical results: (1) The MIB-MRTD method is stable for any M. (2) The MIB-MRTD can achieve better accuracy when M is large and $L \leq 7$ as the standard high-order FDTD method.

The presence of spurious modes is a cause of the instability of the MIB-MRTD method for the hyperbolic $Eq(4.1.1)$. As we discussed above, the eigenvalues of a anti-symmetric matrix are all complex. We thus define the spurious modes as eigenvalues with non-zero real part [**42**]. To detect spurious modes numerically, we examine the largest real part, $\max\{\mathrm{Re}(\lambda)\}$ of the discrete spectrum of the MIB-MRTD method for different M and L values. By setting $N = 100$, these results are listed in $Table(1)$. It can be observed from

TABLE 1. Spectral Radius of MIB-MRTD Matrix

	MIB-MRTD		MIB-FDTD	
		M=3		
L	min[Im(λ)]	max[Re(λ)]	min[Im(λ)]	max[Re(λ)]
1	-2.67(+2)	0	-2.48(+2)	0
2	-2.67(+2)	0	-2.48(+2)	0
3	-2.67(+2)	0	-2.48(+2)	0
4	-2.67(+2)	0	-2.48(+2)	0
5	-2.67(+2)	0	-2.48(+2)	0
6	-2.67(+2)	0	-2.48(+2)	0
7	-2.67(+2)	0	-2.48(+2)	0
8	-2.67(+2)	1.15(+1)	-2.48(+2)	8.82(+0)
9	-2.67(+2)	2.58(+1)	-2.48(+2)	2.16(+1)
10	-2.67(+2)	4.05(+1)	-2.48(+2)	3.31(+1)
		M=5		
L	min[Im(λ)]	max[Re(λ)]	min[Im(λ)]	max[Re(λ)]
1	-2.92(+2)	0	-2.63(+2)	0
2	-2.92(+2)	0	-2.63(+2)	0
3	-2.92(+2)	0	-2.63(+2)	0
4	-2.92(+2)	0	-2.63(+2)	0
5	-2.92(+2)	0	-2.63(+2)	0
6	-2.92(+2)	0	-2.63(+2)	0
7	-2.92(+2)	1.10(-6)	-2.63(+2)	0
8	-2.92(+2)	1.98(+0)	-2.63(+2)	6.73(+0)
9	-2.92(+2)	8.16(+0)	-2.63(+2)	1.85(+1)
10	-2.92(+2)	1.22(+1)	-2.63(+2)	2.88(+1)
		M=7		
L	min[Im(λ)]	max[Re(λ)]	min[Im(λ)]	max[Re(λ)]
1	-3.03(+2)	0	-2.71(+2)	0
2	-3.03(+2)	0	-2.71(+2)	0
3	-3.03(+2)	0	-2.71(+2)	0
4	-3.03(+2)	0	-2.71(+2)	0
5	-3.03(+2)	0	-2.71(+2)	0
6	-3.03(+2)	0	-2.71(+2)	0
7	-3.03(+2)	0	-2.71(+2)	0
8	-3.03(+2)	4.78(+0)	-2.71(+2)	6.23(+0)
9	-3.03(+2)	1.69(+1)	-2.71(+2)	1.80(+1)
10	-3.03(+2)	2.90(+1)	-2.71(+2)	2.84(+1)

Table(1) that for each M, when L is small, all real parts of the discrete spectrum are equal to zero. However, when L is considerably large, some eigenvalues present positive real parts which indicate the presence of spurious modes. It is clear from *Fig*(5.3). that such spurious

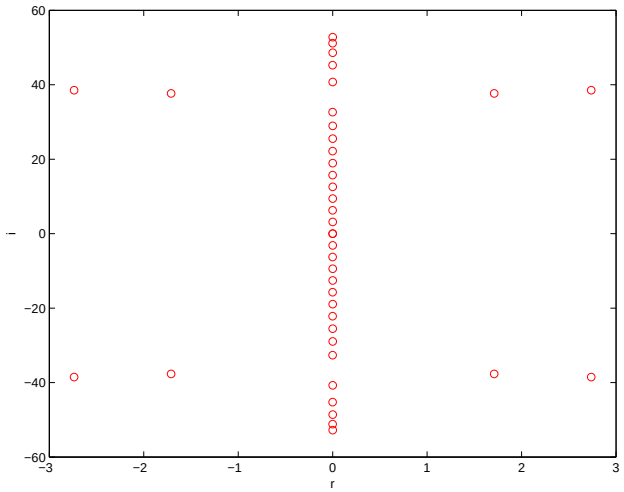

FIGURE 5.5. Spurious Modes

TABLE 2. CFL Number for One Dimensional Wave Equation

M	MIB-MRTD	FDTD	N_t	L
3	1.072386	1.146132	939	$1, \cdots, 7$
5	0.977995	1.081081	1028	$1, \cdots, 7$
7	0.945626	1.052632	1068	$1, \cdots, 7$

modes will be outside of the RK4 stable region unless $\Delta t \to 0$. Therefore, the MIB-MRTD method will be unstable for the hyperbolic equation when the spurious modes occur. $Fig(5.5)$ is an plotting of the eigenvalues for A with $M = 3$ and $L = 9$. It can be seen that four spurious modes are laid out symmetrically on two sides of the complex axis.

After the determination of the spectral radius of A, we are able to numerically calculate the CFL numbers. For the one-dimensional *Maxwell's* equations (2.4.1), we consider a time integration in the range $t \in [0, T]$ with a time increment Δt. Denote the total number of time steps to be N_t. We have $N_t = \frac{T}{\Delta t}$. We numerically search for the critical N_t such that the computation is still stable. Specifically, we choose $\Delta x = 0.01$ and $T = 10$. The results are presented in $Table(2)$. For example, we have $N_t = 1068$ in the third case and for the same M value, we can find the corresponding $|\lambda| = 303$ in $Table(1)$. Thus $\Delta t \cdot |\lambda| = \frac{10}{1068} \cdot 303 \approx 2.83$. Along the complex axis, the RK4 converges if $|\Delta t \cdot \lambda| \leq 2\sqrt{2} \approx 2.83$. It can be seen that the numerical results we found perfectly match the convergent requirements of RK4.

CHAPTER 6

NUMERICAL EXPERIMENTS

In this chapter, we examine the usefulness of the MIB boundary treatment by testing its robustness, accuracy, and convergence. Three MRTD schemes, the CDF(2,2), CDF(2,4), and CDF(2,6), are employed for the spatial discretization and the classical fourth order Runge-Kutta method is used for the temporal integration. Based on some given initial values at time $t = 0$, Maxwell's equations $Eq(3.2.2)$ and $Eq(3.2.4)$ are solved until a stopping time $t = T$. Here we choose $T = 1$ for all tests in our non-dimensionalized unit system. A uniform grid is employed in all examples, with $N+1$ being the mesh size along each direction. Unless otherwise specified, a small time increment $\Delta t = 10^{-4}$ is used to ensure that the temporal discretization error is negligible in our present tests. The absolute L_2 errors are reported in all cases. Denoting u_h as the numerical solution and u is a reference solution, we will report the L_2 error is calculated as the follows: $L_2 = \sqrt{\sum_{i=0}^{N} |u - u_h|^2 / N}$.

6.1. A Hollow Rectangular Waveguide

We first validate the MIB boundary closure scheme by considering an air filled rectangular waveguide with perfect conducting walls as shown in [**32**] in $Fig(6.1)$. Designed to solve complicated boundary conditions, the MIB boundary closure scheme can also handle the simple PEC boundary conditions. Moreover, such a study actually enables us to compare the MIB boundary method with the image principle.

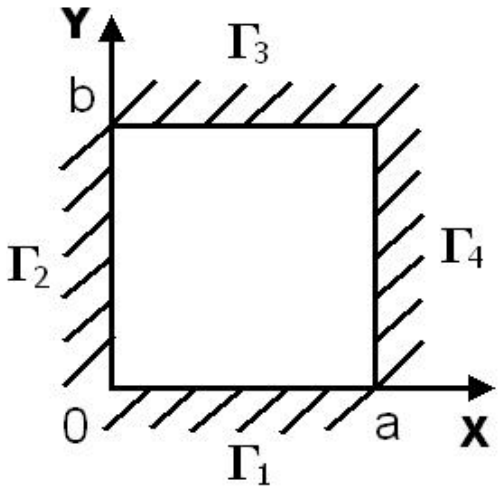

FIGURE 6.1. Perfect Electric Conductor

The cross section of the hollow waveguide is chosen as $(x, y) \in [0, a] \times [0, b]$. Such a simple structure permits analytical solutions:

$$\begin{aligned} E_z &= \sin(\frac{m\pi}{a}x)\sin(\frac{n\pi}{b}y)\cos(\omega t) \\ H_x &= -\frac{n\pi}{\mu\omega b}\sin(\frac{m\pi}{a}x)\cos(\frac{n\pi}{b}y)\sin(\omega t) \\ H_y &= \frac{m\pi}{\mu\omega a}\cos(\frac{m\pi}{a}x)\sin(\frac{n\pi}{b}y)\sin(\omega t) \end{aligned} \tag{6.1.1}$$

where $\omega = \frac{1}{\sqrt{\mu\epsilon}}\sqrt{(\frac{m\pi}{a})^2 + (\frac{n\pi}{b})^2}$, and m and n are the wavenumbers. For the present example, two PEC conditions for magnetic components are used: $\frac{\partial H_y}{\partial x} = 0$ at $x = 0$ and $x = a$, and $\frac{\partial H_x}{\partial y} = 0$ at $y = 0$ and $y = b$. For E_z, we set $E_z = 0$ at the four PEC walls. According to Maxwell's equations, it is easy to derive two electric PEC conditions: $\frac{\partial^2 E_z}{\partial x^2} = 0$ at $x = 0$ and $x = a$, and $\frac{\partial^2 E_z}{\partial y^2} = 0$ at $y = 0$ and $y = b$. With little modification, the MIB treatment discussed in the previous section can be applied to solve these four PEC conditions.

In the present computations, the initial values are taken according to the analytical solutions. The physical parameters are chosen as $a = b = 1$ and $\epsilon = \mu = 1$. Two test cases are examined with $m = n = 5$ in Case 1 and $m = n = 10$ in Case 2. The high frequency solutions in Case 2 are particularly important to investigate the performance of high order

TABLE 1. The MRTD results of Example 1 by using the image principle.

Scheme	Case 1	$N = 20$	$N = 40$	$N = 80$
CDF(2,2)	Error	1.482(−3)	1.116(−4)	7.339(−6)
	Order		3.73	3.93
CDF(2,4)	Error	4.330(−4)	8.110(−6)	1.330(−7)
	Order		5.74	5.93
CDF(2,6)	Error	7.832(−5)	3.771(−7)	1.785(−9)
	Order		7.70	7.72
	Case 2	$N = 20$	$N = 40$	$N = 80$
CDF(2,2)	Error	2.641(−2)	3.689(−3)	2.737(−4)
	Order		2.84	3.75
CDF(2,4)	Error	3.461(−2)	1.075(−3)	1.989(−5)
	Order		5.01	5.76
CDF(2,6)	Error	2.180(−2)	1.944(−4)	9.248(−7)
	Order		6.77	7.75

Here 1.482(−3) denotes 1.482×10^{-3}. In Case 1, $m = n = 5$ and in Case 2, $m = n = 10$.

TABLE 2. The MRTD results of Example 1 by using the MIB scheme.

Scheme	Case 1	$N = 20$	$N = 40$	$N = 80$
CDF(2,2)	Error	1.212(−3)	1.036(−4)	7.096(−6)
	Order		3.55	3.87
CDF(2,4)	Error	3.623(−4)	7.405(−6)	1.274(−7)
	Order		5.61	5.86
CDF(2,6)	Error	5.623(−5)	3.012(−7)	1.968(−9)
	Order		7.54	7.26
	Case 2	$N = 20$	$N = 40$	$N = 80$
CDF(2,2)	Error	2.092(−2)	3.363(−3)	2.638(−4)
	Order		2.64	3.67
CDF(2,4)	Error	2.761(−2)	9.860(−4)	1.903(−5)
	Order		4.81	5.70
CDF(2,6)	Error	2.418(−2)	1.663(−4)	8.326(−7)
	Order		7.18	7.64

In Case 1, $m = n = 5$ and in Case 2, $m = n = 10$.

methods. The numerical results of the image principle and the MIB boundary scheme are listed, respectively, in $Table(1)$ and $Table(2)$.

The image principle is obviously satisfied for the present analytical solutions $Eq(6.1.1)$. Thus, the numerical errors reported in Table 1 are primarily due to the MRTD spatial discretizations. As mentioned above, the order of accuracy for the CDF(2,2),

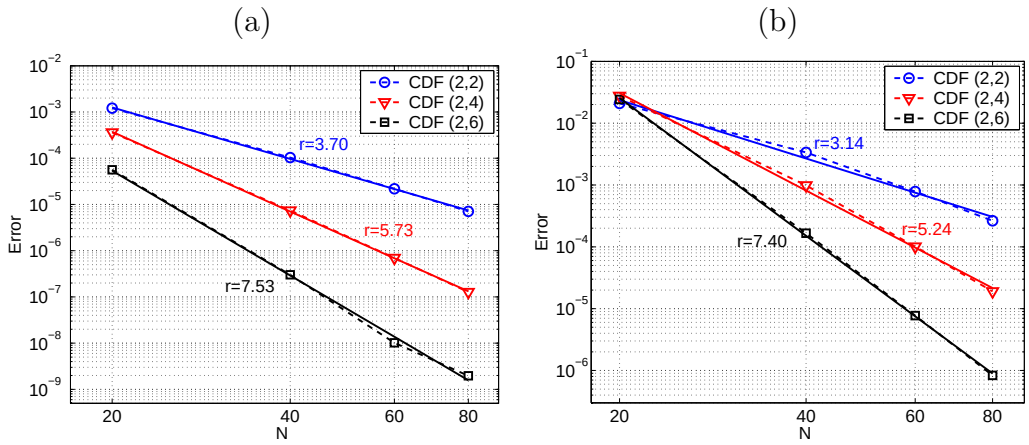

FIGURE 6.2. Numerical convergence rates of the MIB-MRTD method.(a) Example 1, Case 1. (b) Example 1, Case 2.

CDF(2,4), and CDF(2,6) MRTD schemes is, respectively, four, six, and eight. Such orders have been numerically verified for the low and high frequency cases with a large N. Moreover, the order of the computational method is greater than the order of the finite difference scheme for the CDF(2,6) in Case 1, while the CDF(2,6) correctly displays its order in Case 2 with $N = 80$.

With the confidence of the present MRTD spatial discretization, we now turn to the MIB boundary closure. A large enough L is used in the MIB scheme. In particular, we choose $L = 3$, 5, and 7, respectively, for the CDF(2,2), CDF(2,4), and CDF(2,6) MRTD schemes. It can seen from $Table(2)$ that the MIB results are in good agreement with those of the image principle, with very minor differences. This validates the MIB boundary closure scheme for this type of problem.

We further examine the order of convergence of the MIB-MRTD spatial discretization by plotting the numerical errors in charts (a) and (b) of $Fig(6.2)$. These errors are shown as dashed lines. A linear fitting by means of least squares is then conducted for each case in the log-log scale and the corresponding fitted convergence lines are depicted as solid lines in $Fig(6.2)$. Moreover, the fitted slope essentially represents the numerical convergence rate r of the MIB-MRTD method. These rates are shown in $Fig(6.2)$ too. It is interesting to note that there are some differences between the convergence patterns of the low frequency test

(Case 1) and the high frequency test (Case 2). It is known that the high frequency test is challenging to low order methods or coarse numerical meshes [**28**]. Thus, the overall rate of CDF(2,2) for Case 2 is only $r = 3.14$, although it attains a value of 3.67 when $N = 80$ in Table 2. On the other hand, with $N = 20$, all three MRTD schemes perform poorly. The higher order method yields a larger error. This is because the grid resolution is too low in this case, i.e., only 4 grid points per wavelength (PPW). With such a low PPW, only spectral type methods, such as pseudospectral time-domain (PSTD) methods [**29, 30**] or local spectral time-domain (LSTD) methods [**31, 32**], can deliver reasonable accuracy. For the present problem, the MRTD methods perform better when N is larger. Eventually, the numerical orders of both the CDF(2,4) the CDF(2,6) are quite close to the theoretical ones.

$Fig(6.3)$ shows snap shots of E_z in Example(1) at different time steps. All graphs are generated by Matlab using the numerical results we obtained before. It is clear to see that the electric wave is oscillating periodically in the computational domain and its amplitude is determined by $|cos(\omega t)|$.

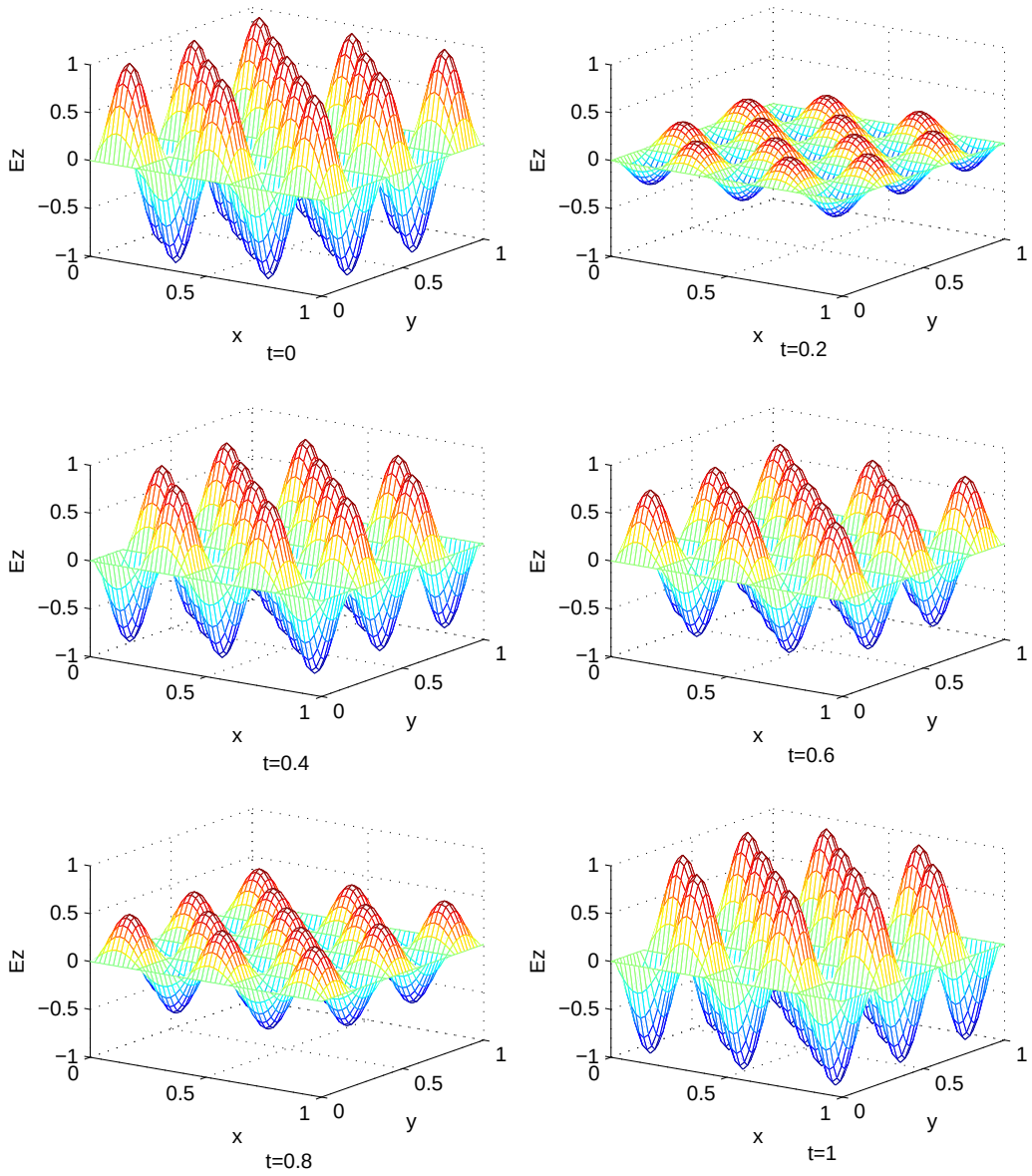

FIGURE 6.3. Matlab Simulation of E_z for $m = 5$,$n = 5$ in Example 1

6.2. A Shifted Computational Domain

We next study a synthetic example based on the hollow rectangular waveguide. Consider the same physical setting as in Example 1, but with a shifted computational domain $(x, y) \in [0, \frac{3}{4}a] \times [0, \frac{4}{5}b]$. Denote four boundaries of this new domain to be Γ_1, Γ_2, Γ_3, and Γ_4,

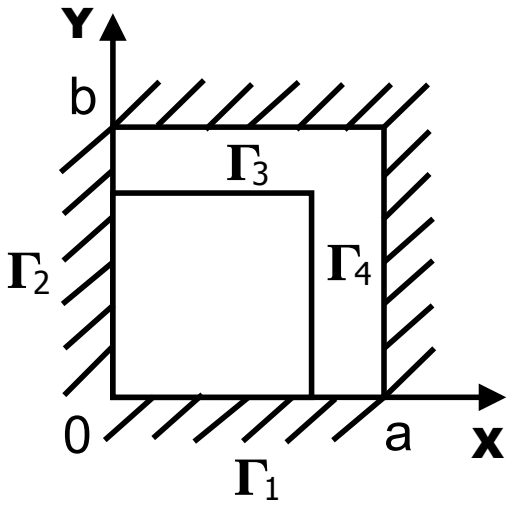

FIGURE 6.4. Shifted Computational Domain

as shown in $Fig(6.4)$. We then have that the PEC conditions are not valid on Γ_3 and Γ_4, although the same analytical solutions are assumed. Instead, the correct boundary conditions are constructed as follows:

$$\frac{\partial^2 E_z}{\partial x^2} + (\frac{m\pi}{a})^2 E_z = 0, \quad \text{on} \quad \Gamma_4 \tag{6.2.1}$$

$$\frac{\partial^2 E_z}{\partial y^2} + (\frac{n\pi}{b})^2 E_z = 0, \quad \text{on} \quad \Gamma_3 \tag{6.2.2}$$

$$\frac{\partial^2 H_y}{\partial x^2} + (\frac{m\pi}{a})^2 H_y = 0, \quad \text{on} \quad \Gamma_4 \tag{6.2.3}$$

$$\frac{\partial^2 H_x}{\partial y^2} + (\frac{n\pi}{a})^2 H_x = 0, \quad \text{on} \quad \Gamma_3 \tag{6.2.4}$$

The image principle obviously cannot handle these complicated boundary conditions.

The MIB treatment of two E_z conditions $Eqs(6.2.1)$ and $(6.2.2)$ can be carried out in a similar fashion. Nevertheless, a subtle point needs to be taken into account in solving magnetic boundary conditions $Eqs(6.2.3)$ and $(6.2.4)$. We illustrate this by considering $Eq(6.2.3)$ as an example. By using a staggered grid, there is actually no grid node for H_y located on the boundary at $x = \frac{3}{4}a$. Thus, the second term in $Eq(6.2.3)$, i.e., $(\frac{m\pi}{a})^2 H_y$, cannot be directly evaluated in the MIB discretization. Instead, the H_y value is interpolated based on the same grid stencil used for approximating the second derivative. In this manner,

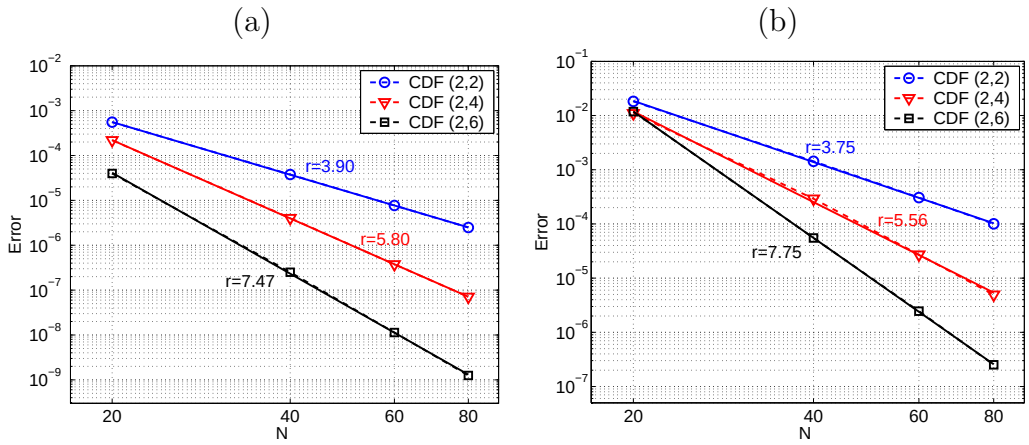

FIGURE 6.5. Numerical convergence rates of the MIB-MRTD method.(a) Example 2, Case 1. (b) Example 2, Case 2.

one may proceed with the MIB scheme as in the previous studies. We note that even though H_x and H_y are time dependent, the MIB representation coefficients solved from boundary conditions $Eq(6.2.3)$ and $Eq(6.2.4)$ are still time independent. Thus, one needs to conduct the MIB treatment only once.

The numerical results of the MIB-MRTD method are reported in $Table(3)$. These results are also depicted in charts (a) and (b) of $Fig(6.5)$. It can be seen that the MIB-MRTD schemes attain the correct numerical orders for both low and high frequency tests. Furthermore, the convergence patterns of the high frequency case become better, in comparison with those of Example 1. This is because a smaller computation domain in Example 2 actually implies a larger PPW. The present result shows that the overall performance of the MIB scheme in handling complicated boundaries is satisfactory.

TABLE 3. The results of the MIB-MRTD method for Example 2.

Scheme	Case 1	$N = 20$	$N = 40$	$N = 80$
CDF(2,2)	Error	5.544(−4)	3.770(−5)	2.486(−6)
	Order		3.88	3.92
CDF(2,4)	Error	2.186(−4)	4.036(−6)	7.078(−8)
	Order		5.76	5.83
CDF(2,6)	Error	3.977(−5)	2.502(−7)	1.251(−9)
	Order		7.31	7.64
	Case 2	$N = 20$	$N = 40$	$N = 80$
CDF(2,2)	Error	1.825(−2)	1.431(−3)	1.003(−4)
	Order		3.68	3.83
CDF(2,4)	Error	1.101(−2)	2.920(−4)	4.951(−6)
	Order		5.24	5.88
CDF(2,6)	Error	1.179(−2)	5.506(−5)	2.513(−7)
	Order		7.74	7.78

In Case 1, $m = n = 5$ and in Case 2, $m = n = 10$.

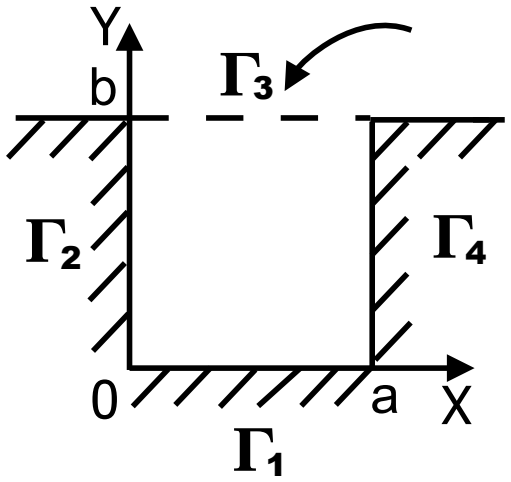

FIGURE 6.6. An Open Cavity

6.3. A Rectangular Open Cavity

Next, we consider a 2D rectangular open cavity embedded in an infinite ground plane, as shown in *Fig*(6.6). The study of electromagnetic scattering by such a cavity is of great industrial and military interest, because the open cavity can be regarded as a prototype structure of a more realistic one, such as a jet engine inlet duct or exhaust nozzle [**40**]. Denote the width of the cavity as a and the depth as b. The cavity walls and ground plane are usually assumed to be PEC boundaries. The problem is defined on the cavity and the half

space above the ground plane with Sommerfeld's radiation conditions imposed at infinity:

$$\lim_{r\to\infty}\left(\frac{\partial u}{\partial N}-iku\right)=0 \tag{6.3.1}$$

where r is the distance the radiating wave travels over time, $\frac{\partial}{\partial N}$ is the normal derivative of the function, and k is the wavenumber. Together with the PEC boundaries, the solution could be expanded as:

$$u(x,y)=\sum_{n=1}^{\infty}\alpha_n\sin\left(\frac{n\pi x}{a}\right)\sinh(k_n y) \tag{6.3.2}$$

where n is an integer, α_n is a constant, and $k_n=\sqrt{(\frac{n\pi}{a})^2-k^2\epsilon\mu}$. A modern approach to solve this problem is to introduce a transparent boundary condition, which serves equivalently as a PML boundary in this case, above the cavity [**40**], along Γ_3 in $Fig(6.6)$.

In the present study, we numerically solve the two-dimensional Maxwell's equations, $Eq(3.2.2)$ and (3.2.4) within the rectangular cavity. To benchmark our numerical results, a set of analytical solutions is constructed as follows:

$$\begin{aligned}
E_z &= \sin(\frac{n\pi}{a}x)\sinh(k_1 y)\cos(\omega t)\\
H_x &= -\frac{k_1}{\mu\omega}\sin(\frac{n\pi}{a}x)\cosh(k_1 y)\sin(\omega t)\\
H_y &= \frac{n\pi}{\mu\omega a}\cos(\frac{n\pi}{a}x)\sinh(k_1 y)\sin(\omega t)
\end{aligned} \tag{6.3.3}$$

where $\omega=\frac{1}{\sqrt{\mu\epsilon}}\sqrt{(\frac{n\pi}{a})^2-k_1^2}$, and n and k_1 are the wavenumbers. Note that the time harmonic part of the analytical solution $Eq(6.3.3)$ actually represents a single mode of the mode-matching solution which converges to the exact solution of the scattering problem [**40**]. Let $e^{-iky}=e^{-k_1 y}$, with the PEC conditions on Γ_1, Γ_2, and Γ_4, the Robin type boundary conditions are assumed on Γ_3:

$$\frac{\partial E_z}{\partial y}-k_1 E_z=k_1\sin(\frac{n\pi x}{a})\cos(\omega t)e^{-k_1 b}, \tag{6.3.4}$$

$$\frac{\partial H_x}{\partial y}-k_1 H_x=\frac{k_1^2}{\mu\omega}\sin(\frac{n\pi x}{a})\sin(\omega t)e^{-k_1 b}. \tag{6.3.5}$$

TABLE 4. The results of the MIB-MRTD method for Example 3.

Scheme	Case 1	$N = 20$	$N = 40$	$N = 80$
CDF(2,2)	Error	1.059(−3)	8.537(−5)	5.764(−6)
	Order		3.63	3.89
CDF(2,4)	Error	3.081(−4)	6.109(−6)	1.035(−7)
	Order		5.66	5.88
CDF(2,6)	Error	5.151(−5)	2.602(−7)	1.594(−9)
	Order		7.63	7.35
	Case 2	$N = 20$	$N = 40$	$N = 80$
CDF(2,2)	Error	2.885(−1)	1.552(−2)	5.663(−4)
	Order		4.22	4.78
CDF(2,4)	Error	2.874(−1)	3.183(−3)	3.400(−5)
	Order		6.50	6.55
CDF(2,6)	Error	2.719(−1)	1.104(−3)	4.395(−6)
	Order		7.94	7.97

In Case 1, $n = 5$ and $k_1 = 1$ and in Case 2, $n = 10$ and $k_1 = 5$.

The terms on the right-hand side of $Eqs(6.3.4)$ and (6.3.5) will eventually decay to 0 because the term $e^{-k_1 y} = 0$ as $y \to \infty$. However, in this case, we only consider the domain for $0 \leq y \leq b$, thus $e^{-k_1 y} = e^{-k_1 b}$ at $y = b$.

The MIB scheme for conditions given by $Eqs(6.3.4)$ and (6.3.5) can be carried out exactly as described in Chapter 3. We note that even though the boundary data ϕ varies along the boundary and is time dependent, i.e., $\phi(x, t)$, the MIB representation coefficients solved from the boundary conditions $Eqs(6.3.4)$ and (6.3.5) are still time and space independent. Thus, it is sufficient to conduct the MIB treatment only once. The solved representation coefficients can then be applied at any time t and at any x node along Γ_3. Therefore, the MIB boundary treatment is computationally very efficient.

In the present study, the physical parameters are chosen as $a = b = 1$ and $\epsilon = \mu = 1$. Again, two test cases are studied with $n = 5$ and $k_1 = 1$ in Case 1 and $n = 10$ and $k_1 = 5$ in Case 2. The numerical results are shown in Table 4 and chart (a) and (b) of $Fig(6.7)$. It can be seen from $Fig(6.7)$ that the correct spatial order of accuracy is achieved in all tests. We note that the MRTD errors are greater than 0.2 when $N = 20$ for the high frequency case. This is because the present solution is highly oscillatory along the x direction, while it is subject to a very rapid exponential growth along the y direction. Such a solution is very

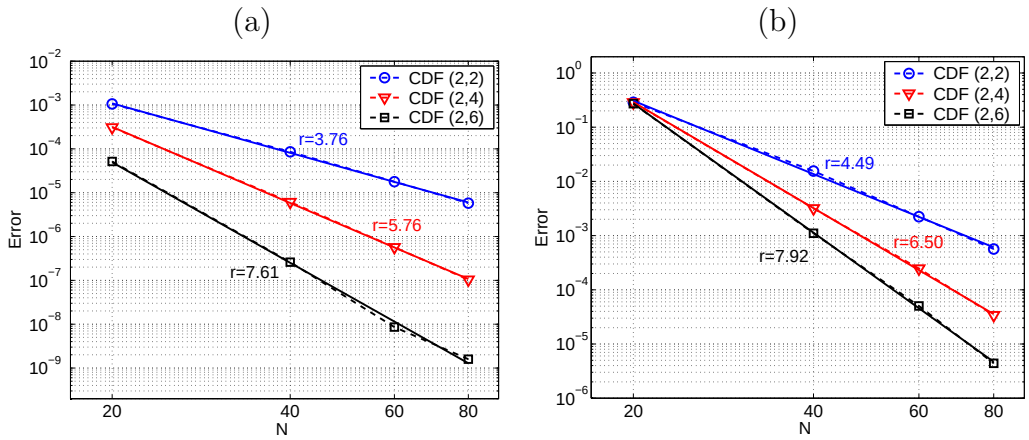

FIGURE 6.7. Numerical convergence rates of the MIB-MRTD method.(a) Example 3, Case 1. (b) Example 3, Case 2.

difficult to be resolved on a coarse grid. Nevertheless, when we refine the mesh, satisfactory accuracy is achieved by the MIB-MRTD scheme.

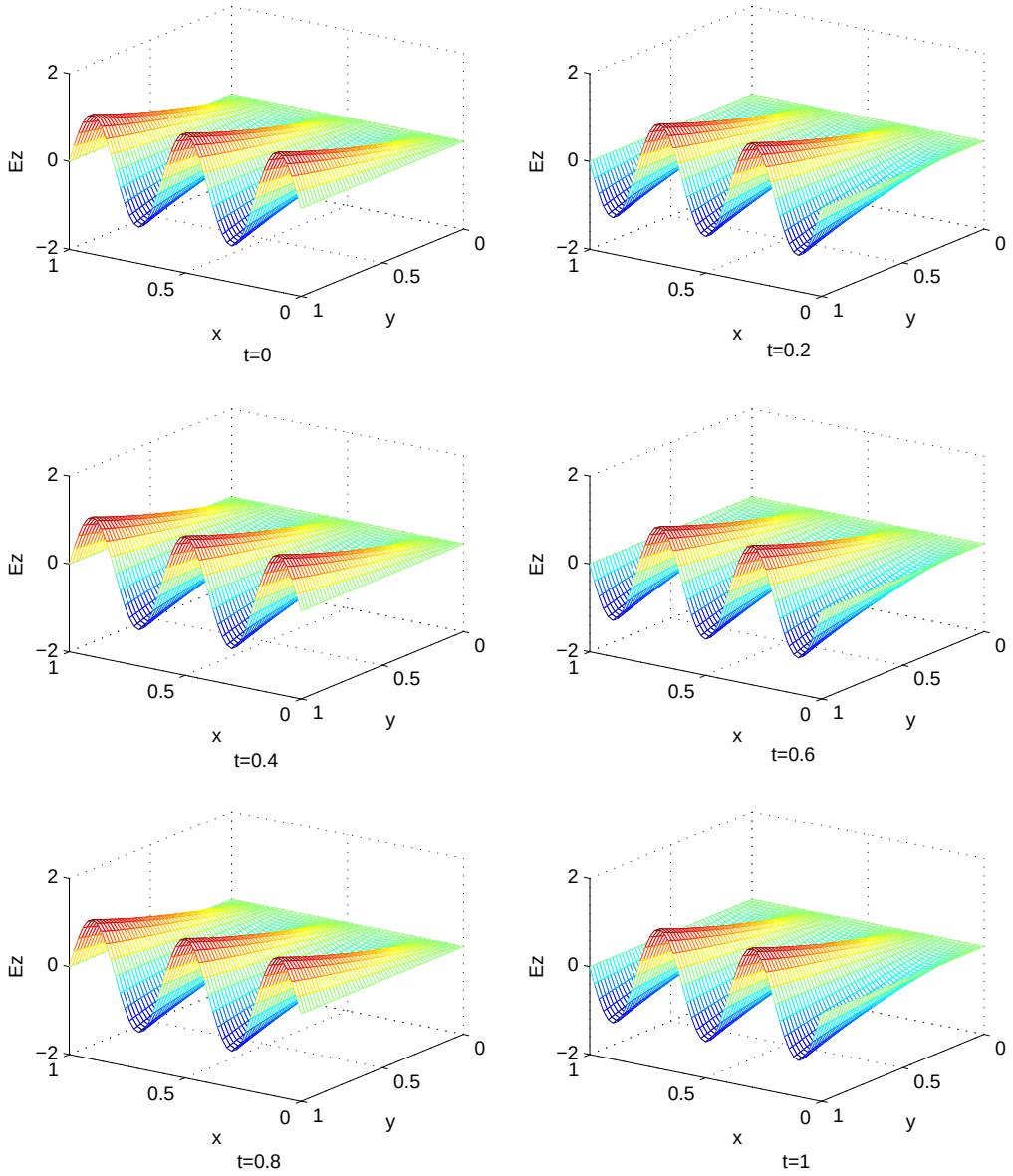

FIGURE 6.8. Matlab Simulation of E_z for n=5, k_1=1 in Example 3

6.4. A Test Without An Analytical Solution

We finally consider a test without an analytical solution. The hollow rectangular waveguide with four PEC boundaries in Example 1 is studied again. However, we consider

TABLE 5. The results of the MIB-MRTD method for Example 4.

Scheme	Case 1	$N = 30$	$N = 60$	$N = 120$
CDF(2,2)	Error	4.633(−3)	5.669(−4)	4.155(−5)
	Order		3.03	3.77
CDF(2,4)	Error	4.928(−3)	1.602(−4)	3.036(−6)
	Order		4.94	5.72
CDF(2,6)	Error	3.056(−3)	3.435(−5)	1.832(−7)
	Order		6.48	7.55
	Case 2	$N = 30$	$N = 60$	$N = 120$
CDF(2,2)	Error	8.255(−3)	1.154(−3)	8.840(−5)
	Order		2.84	3.71
CDF(2,4)	Error	1.005(−2)	4.218(−4)	8.731(−6)
	Order		4.57	5.59
CDF(2,6)	Error	7.225(−3)	1.277(−4)	7.744(−7)
	Order		5.82	7.37

the structure being initially excited by *Gaussian* type pulses. Such a study can be used to numerically predict the cutoff frequencies of the structure [**32**]. A cutoff frequency structure is a boundary only allows propagating waves with certain frequencies to pass. The "unwanted" waves will be attenuated or reflected at the boundary.

Two initial values of E_z are considered:

$$E_z(x, y, 0) = Ae^{-\frac{(x-\frac{a}{2})^2+(y-\frac{b}{2})^2}{2\sigma^2}}, \tag{6.4.1}$$

$$E_z(x, y, 0) = Ae^{-\frac{(x-\frac{a}{2})^2+(y-\frac{b}{2})^2}{2\sigma^2}} \sin(\frac{5\pi}{a}x) \sin(\frac{5\pi}{b}x), \tag{6.4.2}$$

respectively, for Cases 1 and 2, while the initial values of H_x and H_y are chosen as zero. Here $a = b = 1$, $A = 10$, and $\sigma = 0.05$. The PEC conditions hold in Case 2, while the initial solution of Case 1 satisfies the PEC conditions approximately, since the *Gaussian* decays to a negligibly small values at the boundaries. We then integrate Maxwell's equations to $T = 1$. No analytical solution is available to benchmark our MIB results. Thus, an "exact solution" obtained by the MIB-MRTD with CDF(2,6) and a dense mesh $N = 240$ is used as the reference. In comparing with the reference solution, the MIB-MRTD errors are shown in $Table(5)$ and charts (a) and (b) of $Fig(6.9)$. It can be seen that the correct orders are numerically achieved.

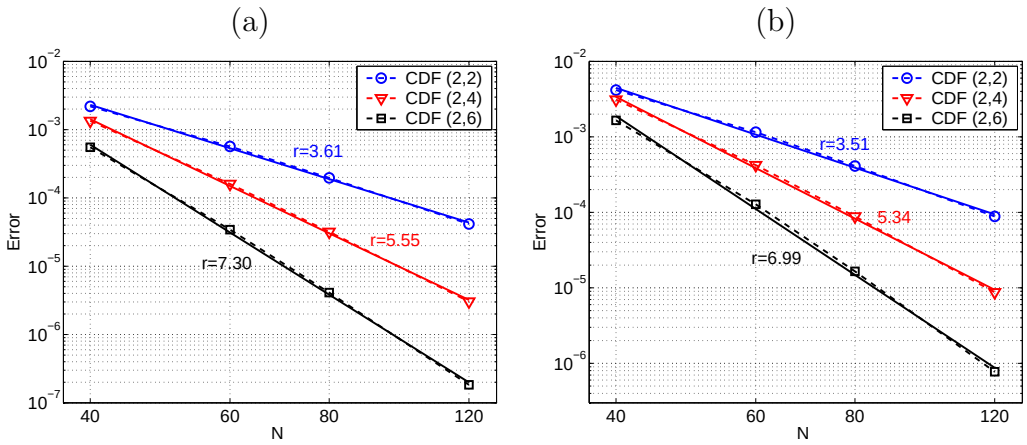

FIGURE 6.9. Numerical convergence rates of the MIB-MRTD method.(a) Example 4, Case 1. (b) Example 4, Case 2.

In this example, a *Gaussian* pulse occurs at the center of the computational domain. It starts to propagate both in the $x-$ and $y-$ directions under the governing of *Maxwell's* equations. A sinusoidal oscillation around the origin can be clearly observed. The outgoing wave first reaches and then bounds back from the boundaries after a certain amount of time in a manner defined by the PEC boundary conditions. The outgoing wave and bound-back wave collide and amalgamate with each other since $t \geq 0.6$. A equilibrium state will be achieved for a sufficient large t.

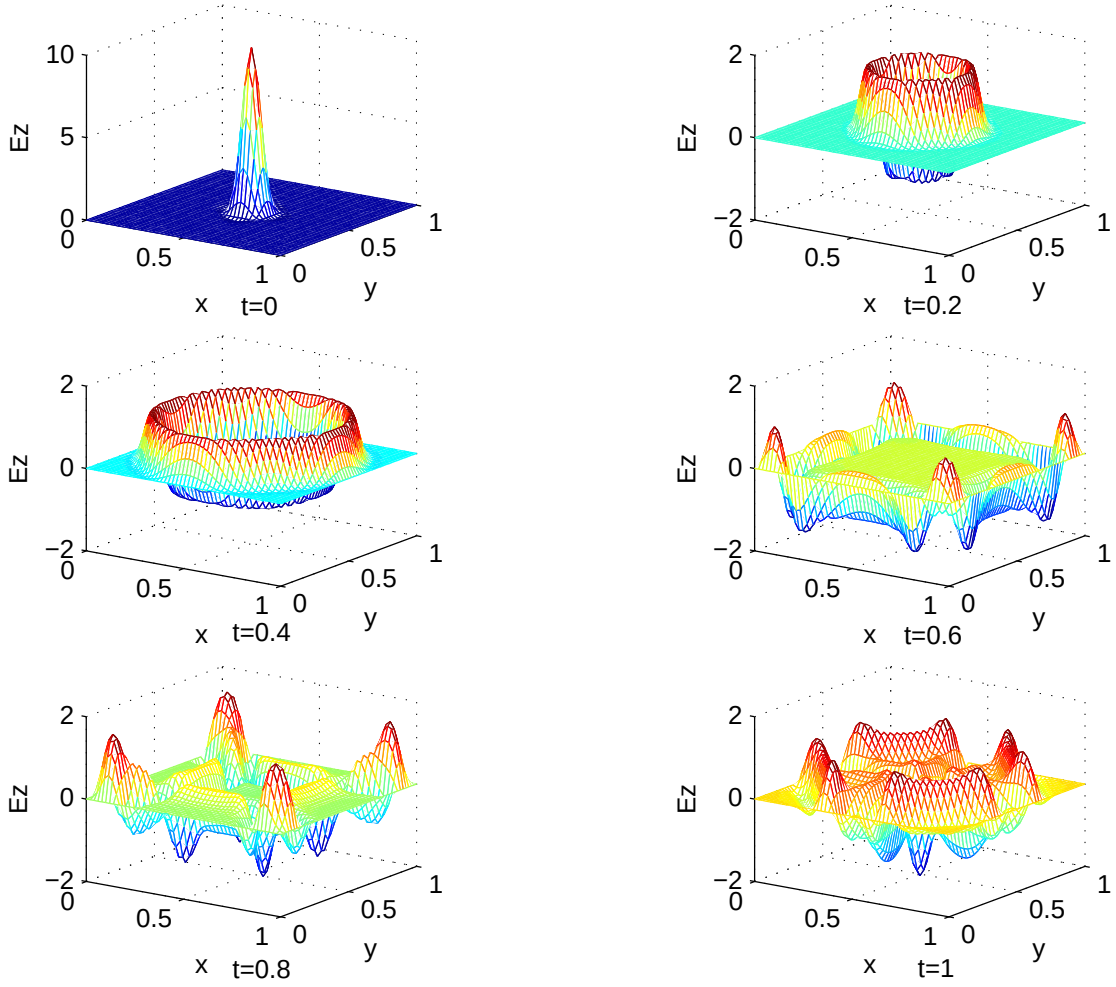

FIGURE 6.10. Matlab Simulation of E_z for A=10 and $\sigma = 0.05$ in Example 4

CHAPTER 7

CONCLUSION AND FUTURE WORK

We start with a brief introduction of the historical background of Electromagnetics and *Maxwell's* equations. Several important modes of the *Maxwell's* equations have been presented together with an introduction of the PML, PEC and PMC boundaries conditions that have great importance in practical application. In Chapter 3, we outline the MRTD analysis and compare the advantages and disadvantages of different wavelets. In particular, the discretization coefficients of the Daubechies wavelet are calculated for future use. In the same chapter, we have introduced a new boundary closure scheme, the MIB method, for the treatment of general boundary conditions in the MRTD calculations of *Maxwell's* equations. In the MIB method, boundary conditions are repeatedly utilized to systematically determine a set of fictitious values outside the computational domain. Consequently, the MRTD approximation can be applied in a translation invariant manner near the boundary.

A dispersion analysis is conducted immediately after that for both MIB-FDTD and MIB-MRTD methods. A dispersion relation for Yee's FDTD method is developed. The dispersion error, which is defined as the variation between the numerical wave and physical wave, is caused by insufficient small time and spatial increments in numerical discretization. We can diminish the numerical dispersion error by reducing the time and spatial increments. However, the computational cost could be significantly increased by a more refined mesh. It is of great interest for us to compare the dispersion error for different numerical schemes with same choices of the time and spatial increments. Due to the numerical complexity and loss of matric symmetry, it is extremely difficult to formulate the analytic dispersion relation for the MIB-MRTD method. Thus, we choose to numerically compare the dispersion error of the FDTD and MRTD methods under a frequency domain. It is found that the MRTD method is able to maintain low dispersion error over a broader frequency band.

In chapter 5, a stability analysis for the proposed MIB-MRTD method is conducted from a matrix structure angle. A dicretization matrix of the MIB-MRTD method is constructed and its associated eigenvalues were calculated. The MIB-MRTD method is numerically stable despite the choice of M. It can achieve better accuracy as M increases with L is not too large. The Courant - Friedrichs - Levy (CFL) Numbers have been calculated for both FDTD and MIB-MRTD methods with different choices of M and L. We numerically verify the relation between the spectral radius of the dicretization matrix and the corresponding CFL number.

Several numerical experiments have been carried out to demonstrate the robustness of the MIB scheme in handling complicated boundary conditions, such as Robin and/or time-dependent ones. The MIB boundary treatment can achieve arbitrarily high order accuracy in principle. In the present study, the MIB orders are guaranteed to be not less than that of the underlying MRTD spatial discretization, so that the MIB-MRTD methods achieve the theoretical orders in all numerical tests. The MIB coefficient generation can be carried out only once to deal with boundary conditions with spatial and temporal dependent inhomogeneous terms. Thus, the MIB boundary treatment is computationally cheap. The MIB fictitious domain treatment does not assume any *a priori* knowledge of wave solutions, so that it has no limitation to be applied to real world electromagnetic problems.

The MIB treatment of nontrivial boundary conditions on irregular domains is currently under out consideration. A study of Metamaterial with negative refractive indices will be conducted after completion of the boundary problem. Negative refractive index materials have gained rapid growth interests over the years due to their special optical properties. Metamaterials are artificial materials engineered to have negative refractive indices $n = -\sqrt{\epsilon\mu}$, or permittivity $\epsilon < 0$, permeability $\mu < 0$, respectively. The computational difficulty lies in the interface treatment. Averaging of the material characteristics over a computational cell at the interface between positive and negative material characteristics may lead to zero values of the quantities. Therefore, the classical FD scheme may become

degenerate[**44**]. New interface treatments based on MIB method will be constructed to resolve the difficulty.

Bibliography

[1] Pengfei Yao and Shan Zhao, "A new boundary closure scheme for the multiresolution time-domain (MRTD) method", *IEEE Trans. Antennas Propag.*.

[2] Yee, K.S., "Numerical solution of initial boundary value problems involving Maxwell's equations in isotropic media", *IEEE Trans. Antennas Prop.*,vol. 14, pp.302-307, 1966.

[3] J. Fang, "Time domain finite difference computation for Maxwell's equations", Ph.D. dissertation, (Department of Electrical Engineering, University of California, Berkeley, CA, 1989).

[4] S. Wang, F.L. Teixeira, R. Lee, and J.-F. Lee, "Dispersion-relation-preserving (DRP) 2D finite-difference time-domain schemes", in *Proc. IEEE Antennas Propag. Soc. Int. Symp.*, San Antonio, Tx, Vol 3, pp. 264-267, 2002.

[5] S. Wang and F.L. Teixeira, "Dispersion-relation-preserving (DRP) FDTD algorithms for large-scale three dimensional problems", *IEEE Trans. Antennas Propag.*, Vol 51, pp. 1818-1828, 2003.

[6] R.F. Harrington., "Field computation by moment methods", *Malabar, FL: Krieger*, 1982.

[7] M. Krumpholz and L.P.B. Katehi, "New time-domain schemes based on multiresolution analysis", *IEEE Trans. Microw. Theory Tech.*, Vol 44, pp. 555-571, 1996.

[8] L.P.B. Katehi, J.F. Harvey, and E. Tentzeris, "Time-domain analysis using multiresolution expansions", in *Advances in Computational Electrodynamics: The Finite-Difference Time-Domain Method*, Ed. by A. Taflove, Artech House, Boston, MA, 1998.

[9] X. Wei, E. Li and C. Liang "A new MRTD scheme based on Coifman Scaling functions for the solution of scattering problems", *IEEE Microw. Wireless Compon. Lett.*, vol 12, pp. 392-394, 2002.

[10] M. Fujii and W.J.R. Hoefer, "Time-domain wavelet Galerkin modeling of two-dimensional electrically large dielectric waveguides," *IEEE Trans. Microw. Theory Tech.*, Vol. 49, pp. 886-892, 2001.

[11] T. Dogaru and L. Carin, "Multiresolution time-domain using CDF biorthogonal wavelets," *IEEE Trans. Microw. Theory Tech.*, Vol. 49, pp. 902-912, 2001.

[12] N. Kovvali, W. Lin and L. Carin, "Order of accuracy analysis for multiresolution time-domain using Daubechies bases," *Microw. Opt. Tech. Lett.*, Vol. 45, pp. 290-293, 2005.

[13] Q.S. Cao, R. Kanapady, and F. Reitich, "High-order Runge-Kutta multiresolution time-domain methods for computational electromagnetics," *IEEE Trans. Microw. Theory Tech.*, Vol. 54, pp. 3316-3326, 2006.

[14] J. Berenger, "A perfectly matched layer for the absorption of electromagnetic waves", *J. Comput. Physics* vol. 114, pp. 185C200, 1994.

[15] W.Z. Huang and D.M. Sloan, "The pseudoepectral method for solving differential eigenvalue problems", *J. Comput. Phys.*, vol. 111, pp. 399-409, 1994.

[16] G. W. Wei, Y. B. Zhao and Y. Yang, "Discrete singular convolution and its application to the analysis of plates with internal supports. Part 1: Theory and algorithm", *Inter. J. Numer Meth in Engng*, vol. 55, pp.913-946, 2002.

[17] S. Zhao, "On the spurious solutions in the high-order finite difference methods", *Comput. Method Appl. Mech. Engrg.*, vol 196, pp. 5031-5046, 2007.

[18] S. Zhao and G.W. Wei, "Matched interface and boundary (MIB) method for the implementation of boundary conditions in high-order central finite differences," *Int. J. Numer. Method Engrg.*, vol. 77, pp. 1690-1730, 2009.

[19] S.Zhao and G.W. Wei, "High order FDTD methods via derivative matching for Maxwell's equations with material interfaces", *J. Comput. Phys.*, vol. 200, pp. 60-103, 2004.

[20] S.Zhao and G.W. Wei, "Tensor product derivative matching for wave propagation in inhomogeneous media", *Microwave and Optical Technology Letters*, vol. 43, pp. 69-77, 2004.

[21] S. Zhao, "High order vectorial analysis of waveguides with curved dielectric interfaces", *IEEE Microw. Wireless Compon. Lett.*, vol 19, pp. 266-268, 2009.

[22] R.J. LeVeque and Z.L. Li, "The immersed interface method for elliptic equations with discontinuous coefficients and singular sources", *SIAM J. Numer. Anal*, vol. 31, pp. 1019-1044, 1994.

[23] Benjamin Franklin (January 17, 1706 C April 17, 1790) was one of the Founding Fathers of the United States of America. A noted polymath. As a scientist, he was a major figure in the American Enlightenment and the history of physics for his discoveries and theories regarding electricity.

[24] Ismo V. Lindell "Transformation Method for Problems Involving Perfect Electromagnetic Conductor (PEMC) Structures", *IEEE Trans. Antennas Prop.*, vol.53, pp. 3005-3011, 2005.

[25] J.R. Williams and K. Amaratunga, "Introduction to wavelet in engineering", *Int. J. Numer. Methods Eng.*, vol. 37, pp. 2365-2388, 1994.

[26] E.M. Tentzeris, R.L. Robertson, J.F. Harvey, and L.P.B. Katehi, "PML absorbing boundary conditions for the characterization of open microwave circuit components using multiresolution time-domain techniques (MRTD)," *IEEE Trans. Antennas Propag.*, vol. 47, pp. 1709-1715, 1999.

[27] S. Zhao, "High order matched interface and boundary methods for the Helmholtz equation in media with arbitrarily curved interfaces", *J. Comput. Phys.*, vol 229, pp. 3155-3170, 2010.

[28] G. Bao, G.W. Wei, and S. Zhao, "Numerical solution of the Helmholtz equation with high wavenumbers", *Inter. J. Numer. Methods in Engng.*, vol. 59, pp. 389-408, 2004.

[29] Q.H. Liu, "The PSTD algorithm: A time-domain method requiring only two cells per wavelength", *Microw. Opt. Techn. Lett.*, Vol 15, pp. 158-165, 1997.

[30] Q.H. Liu, "Large-scale simulations of electromagnetic and acoustic measurements using the pseudospectral time-domain (PSTD) algorithm", *IEEE Trans. Geosci. Remote Sens.*, Vol 37, pp. 917-926, 1999.

[31] G. Bao, G.W. Wei and S. Zhao, "Local spectral time-domain method for electromagnetic wave propagation", *Opt. Lett.*, Vol 28, pp. 513-515, 2003.

[32] Z.H. Shao, G.W. Wei and S. Zhao, "DSC time-domain solution of Maxwell's equations", *J. Comput. Phys.*, Vol 189, pp. 427-453, 2003.

[33] K.L. Shlager and J.B. Schneider, "Comparison of the dispersion properties of higher order FDTD schemes and equivalent-sized MRTD schemes," *IEEE Trans. Antennas Propag.*, Vol. 52, pp. 1095-1104, 2004.

[34] R. Dautray and J.L. Lions, "Mathematical analysis and numerical methods for science and technology".

[35] A. Taflove and S.C. Hagness, "Computational Electrodynamics: The Finite-Difference Time-Domain Method", 2000.

[36] Q.S. Cao, Y.C. Chen, and R. Mittra, "Multiple image technique (MIT) and anisotropic perfectly matched layer (APML) in implementation of MRTD scheme for boundary truncations of microwave structures," *IEEE Trans. Microw. Theory Tech.*, Vol. 50, pp. 1578-1589, 2002.

[37] M. Peschke and W. Menzel, "Investigation of boundary algorithm for multiresolution analysis," *IEEE Trans. Microw. Theory Tech.*, Vol. 51, pp. 1262-1268, 2003.

[38] N. Kovvali, W. Lin and L. Carin, "Image technique for multiresolution time-domain using nonsymmetric basis functions," *Microw. Opt. Tech. Lett.*, Vol. 47, pp. 44-47, 2005.

[39] S. Zhao, "A fourth order finite difference method for waveguides with curved perfectly conducting boundaries", *Comput. Method Appl. Mech. Engrg.*, vol 199, 2655-2662, 2010.

[40] G. Bao and W. Zhang, "An improved mode-matching method for large cavities", *IEEE Antennas Wireless Propag. Lett.*, vol. 4, pp. 393-396, 2005.

[41] Abbas Alighanbari and Costas.D. Sarris, "Dispersion Properties and Applications of the Coifman Scaling Function Based S-MRTD",*IEEE Trans. Antennas Prop.*, vol. 54, pp. 2316-2325, 2006.

[42] Zhao S., "On the spurious solutions in the high order finite difference methods", *Comput. Methods in App. Mechanics Engng.* vol. 196, pp. 5031C5046, 2007.

[43] V.G. Veselago, "The electrodynamics of substances with simultaneouly negative values of ϵ and μ" 1968.

[44] F. Cajko and I. Tsukerman, "Flexible Approximation Schemes for wave refraction in negative index material", *IEEE Trans. Magn.*, vol. 44 No.6, 2008.

APPENDIX

A. The Finite Difference Method for The One-Dimensional Wave Equation

In one dimensional case, let us consider a *Taylor's* series expansion of $u(x, t_n)$ about the space point x_m to the space point $x_m + \Delta x$, keeping time fixed at t_n [**35**]:

$$u(x_m + \Delta x)|_{t_n} = u|_{x_m,t_n} + \Delta x \cdot \left.\frac{\partial u}{\partial x}\right|_{x_m,t_n} + \frac{(\Delta x)^2}{2} \cdot \left.\frac{\partial^2 u}{\partial x^2}\right|_{x_m,t_n} + \frac{(\Delta x)^3}{6} \cdot \left.\frac{\partial^3 u}{\partial x^3}\right|_{x_m,t_n} + \frac{(\Delta x)^4}{24} \cdot \left.\frac{\partial^4 u}{\partial x^4}\right|_{\xi_1,t_n} \tag{A.1}$$

The last term is the remainder (error). Here, ξ_1 is a space point located somewhere in the interval $(x_m, x_m + \Delta x)$. Similarly, consider the *Taylor's* series expansion to the space point $x_m - \Delta x$, again keeping time fixed at t_n:

$$u(x_m - \Delta x)|_{t_n} = u|_{x_m,t_n} - \Delta x \cdot \left.\frac{\partial u}{\partial x}\right|_{x_m,t_n} + \frac{(\Delta x)^2}{2} \cdot \left.\frac{\partial^2 u}{\partial x^2}\right|_{x_m,t_n} - \frac{(\Delta x)^3}{6} \cdot \left.\frac{\partial^3 u}{\partial x^3}\right|_{x_m,t_n} + \frac{(\Delta x)^4}{24} \cdot \left.\frac{\partial^4 u}{\partial x^4}\right|_{\xi_2,t_n} \tag{A.2}$$

In the remainder term, ξ_2 is a space point located somewhere in the interval $(x_m - \Delta x, x_m)$. Now, adding Eqs(A.1) and (A.2), we obtain:

$$u(x_m + \Delta x)|_{t_n} + u(x_m - \Delta x)|_{t_n} = 2u|_{x_m,t_n} + (\Delta x)^2 \cdot \left.\frac{\partial^2 u}{\partial x^2}\right|_{x_m,t_n} + \frac{(\Delta x)^4}{12} \cdot \left.\frac{\partial^4 u}{\partial x^4}\right|_{\xi_3,t_n} \tag{A.3}$$

Here, by the mean value theorem, ξ_3 is a space point located somewhere in the interval $(x_m - \Delta x, x_m + \Delta x)$. Rearranging terms, we obtain:

$$\left.\frac{\partial^2 u}{\partial x^2}\right|_{x_m,t_m} = \left[\frac{u(x_m + \Delta x) - 2u(x_m) + u(x_m - \Delta x)}{(\Delta x)^2}\right]_{t_n} + O\left[(\Delta x)^2\right] \tag{A.4}$$

where $O\left[(\Delta x)^2\right]$ represents the higher order term which converges to zero at the rate of the square of the space increment. Eq(A.4) is a second-order accurate, central-difference

approximation to the second partial space derivative of u. For convenience, we adopt a subscript m for the space position and a superscript n for the time observation point. Eq(A.4) is rewritten as:

$$\left.\frac{\partial^2 u}{\partial x^2}\right|_{x_m,t_m} = \frac{u_{m+1}^n - 2u_m^n + u_{m-1}^n}{(\Delta x)^2} + O\left[(\Delta x)^2\right] \tag{A.5}$$

For the second partial derivative, we keep x_m fixed and expand u in forward and backward *Taylor's* series in time. By analogy with Eq(A.5), we obtain a second-order accurate, central-difference approximation to the second partial time derivative of u:

$$\left.\frac{\partial^2 u}{\partial t^2}\right|_{x_m,t_m} = \frac{u_m^{n+1} - 2u_m^n + u_m^{n-1}}{(\Delta t)^2} + O\left[(\Delta t)^2\right] \tag{A.6}$$

Substituting the two central-difference expressions of (A.5) and (A.6) into the one-dimensional scalar wave Eq(4.1.1), we have:

$$\frac{u_m^{n+1} - 2u_m^n + u_m^{n-1}}{(\Delta t)^2} + O\left[(\Delta t)^2\right] = c^2\left\{\frac{u_{m+1}^n - 2u_m^n + u_{m-1}^n}{(\Delta x)^2} + O\left[(\Delta x)^2\right]\right\} \tag{A.7}$$

This approximation to the scalar wave equation has a second-order accuracy in both space and time, $O[(\Delta t)^2+(\Delta x)^2]$, which is denoted succinctly as (2,2) accurate solution. Neglecting the *Taylor* series remainder terms and solving for the latest value of u at grid point m, we obtain:

$$u_m^{n+1} = \left(\frac{c\Delta t}{\Delta x}\right)^2\left[u_{m+1}^n - 2u_m^n + u_{m-1}^n\right] + 2u_m^n - u_m^{n-1} \tag{A.8}$$

This is a fully explicit second-order accurate expression for u_m^{n+1} in that all wave quantities on the right-hand side are known; that is they were obtained during the previous time steps, n and $n-1$, and then stored in the computer memory. No simultaneous equation solution is needed, Upon performing Eq(A.8) for all space points of interest, yielding the complete set of u_m^{n+1}, the process can be reapplied to obtain u_m^{n+2}. Repetition of Eq(A.8) over the problem space constitutes the numerical FDTD solution of the scalar wave equation.